

# RIS-aided Passive Detection for LSS Targets: A GNSS Multipath-assisted Scheme

Xuetong Xu, Yang Zhou, Huiying Li, Ao Peng, *Member, IEEE*, Qiang Ye, *Senior Member, IEEE*, and Qi Yang\*, *Member, IEEE*

**Abstract**—The complex topography of urban canyons with many reflectors and scatterers makes it challenging to detect low-altitude, smaller, and slow-speed targets. In this paper, we present a novel multipath-assisted passive detection scheme based on the global navigation satellite system signals in urban canyons. We first propose an information-level target detection scheme, where a binary hypothesis test is conducted according to variation in the received signal given the presence or absence of targets in the environment. To take usage of multipath components (MPCs) in the proposed scheme, we introduce virtual anchors to model reflected signals' propagation paths. We also introduce the reconfigurable intelligent surface to artificially improve the reflective environment and enhance the quality of received MPCs. The detection performance indicators are analyzed theoretically. Simulation results show that the proposed schemes respectively reach 90% and 94% detection probability at a signal-to-noise ratio of 5 dB. The RIS-based method outperforms the multipath-assisted method when the RIS error is less than 0.41 m.

**Index Terms**—Passive detection, GNSS passive radar, multipath-assisted detection, reconfigurable intelligent surface.

## I. INTRODUCTION

**D**ETECTION of low-altitude, smaller size, and slow-speed (LSS) targets represented by unmanned aerial vehicles gains increasing attention and interest in research. Abuses of drones such as smuggling, privacy violations, and espionage occur, and drone terrorist attacks and malicious flight disruptions have tremendous harm [1]. These inappropriate applications threaten public safety. Detection is the first step in dealing with LSS targets threats. Air target detection techniques can be broadly classified as either active or passive. Under active detection, a dedicated transmitter must control the transmitted signal, resulting in high costs and complex operations. Passive detection systems in which opportunity signals act as noncooperative illuminators involve low costs and energy consumption [2], making this approach more effective than active detection. The choice of the illuminator is fundamental to passive detection. Common opportunity signals that can be utilized as illuminators include digital video broadcasting (terrestrial) [3], Wi-Fi [4], long-term evolution [5], and the 5<sup>th</sup> generation wireless systems [6]. These signals

This work was supported in part by the Science and Technology Key Project of Fujian Province under Grant 2021HZ021004, and Fujian Science and technology plan project No.2022I0001. (Corresponding author: Qi Yang)

Xuetong Xu, Yang Zhou, Huiying Li, Ao Peng, and Qi Yang are now with the School of Informatics, Xiamen University, Xiamen, Fujian 361005, China (e-mail: xuxuetong4728@gmail.com; zhouyang1@stu.xmu.edu.cn; li-huiying@stu.xmu.edu.cn; pa@xmu.edu.cn; yangqi@xmu.edu.cn).

Qiang (John) Ye is with the Department of Electrical and Software Engineering, University of Calgary, Calgary, AB T2N 1N4, Canada (e-mail: qiang.ye@ucalgary.ca).

exhibit varying detection ranges and accuracy. Compared with the above illuminators, the global navigation satellite system (GNSS) can provide all-day global coverage due to its constellation design. This system is hence one of the most promising illuminators for passive detection. Using the GNSS as an illuminator offers advantages such as precise synchronizing performance, wideband with modernized signals, and a special microwave region (L-band) to reduce interference. The GNSS-based passive detection is recently employed in vessel target detection [7]–[9]. In [7], multiple GNSS satellites are used to detect and image a vessel target. Image processing is usually modeled as an optimization problem and solved using particle swarm optimization. The authors in [8] analyzed the possibility of identifying moving targets via a GNSS-based passive bistatic radar and verified the approach's feasibility through experiments.

Unlike the open sea, urban canyons have a complex topography containing many reflectors (e.g., large building surfaces) and scatterers (e.g., small irregular objects such as trees). Detecting LSS targets in urban environments is thus more difficult than on the open water. Severe multipath effects also impede adequate detection. Identifying and suppressing multipath clutter in a received signal can mitigate detection errors induced by non-line-of-sight (NLOS) signals [10]–[12]. However, urban canyons possess dense multipath components (MPCs), further hindering identification. Another classic method is shown to enhance detection robustness [12], [13]. However, an accurate priori distribution of MPCs is required, which is challenging to obtain—especially in dense canyons with complex and highly compacted buildings.

Currently, a new multipath-assisted approach emerges, which takes signal propagation parameters of MPCs as additional observations, and then transforms MPCs from impairments to advantages [14]. MPCs attributable to specular reflections account for most MPCs in typical urban canyon scenarios, such as super urbanized cities where the facades of large buildings (e.g., glass, smooth walls) act as reflective surfaces [15]. These MPCs carry rich environmental information. Virtual anchors (VAs), the mirror images of a static receiver or transmitter, are introduced to capitalize on reflected MPCs. In brief, the VAs model reflected MPCs as direct paths between a given detection satellite and a VA. MPC-based information gain is analyzed via the Fisher information matrix in [16]; results confirmed the viability of the multipath-assisted method. A belief propagation-based multipath positioning and mapping algorithm is devised in [17], where a factor graph is used to factorize the joint posterior probability density function

(PDF) and simplify calculation. The multipath-assisted method is useful for sensing as well as positioning. In [18], VAs are created to bridge active and passive sensing and to allow for information fusion. With respect to urban canyons, the model availability of reflected MPCs is verified in [19] based on real-world data. However, there are few research on multipath-assisted target detection in urban canyons.

Building-related obstruction and reflection can severely degrade channel quality within satellite networks in complex urban environments [20], [21]. It is similarly impossible to ignore [22] path loss due to long distance, atmospheric absorption, and near-ground propagation. Reconfigurable intelligent surfaces (RISs) are proposed to address these problems [23] in wireless communication, location, sensing, and other domains [24], [25]. As a novel passive-radio application, a RIS with a vast number of passive elements on a flat surface can manipulate signal propagation by separately adjusting the phase of the impinging signal via each RIS element. An entire RIS's scattering, absorption, reflection, and diffraction properties can be controlled by software to vary with time [26]–[29]. Essentially, a RIS can add controllable paths to complement uncontrollable propagation [30]. Scholars implement RISs in satellite communications to compensate for high path loss, where a RIS is placed on a satellite [31] or user equipment near the ground [23], [32] to promote communication performance. A new RIS-aided low Earth orbit satellite communication system with two-sided cooperative RISs is put forth in [33] to maximize overall channel gain. Overall, RISs offer a promising solution to enhance received signals' quality from an uncontrollable propagation environment and compensate for path loss in satellite-ground networks, particularly in the urban canyons.

In this paper, we present a novel multipath-assisted passive detection scheme based on GNSS signals in urban canyons. An information-level detection scheme using the binary hypothesis test is introduced as a foundation. In the basic scheme, the propagation parameters of MPCs, including amplitude and delay, which can be observed from an M-tap pattern matching filter (PMF), are used to validate the existence of LSS targets. We also introduce VAs into our detection scheme to alleviate multipath effects in urban canyons. The VAs are modeled as the mirror points of the static GNSS receiver according to environmental reflections, and the geographic distribution of the VAs is learned in the offline training phase. The quality of natural reflective surfaces in urban canyons is a key factor in the proposed approach, severely impacting the detection performance. We then introduce RIS in our multipath-assisted scheme to artificially improve the reflective environment. Well-designed RIS deployment can improve the distribution of VAs, and also can enhance the quality of received MPCs. We design the phase shift matrix of the RIS array to optimize the target echo signal, so that the proposed method can provide all-day abnormal LSS target monitoring. All numerical results are consistent with our theoretical analysis.

Our main contributions are summarized as follows:

- 1) A novel multipath-assisted passive detection scheme for urban canyon LSS targets based on GNSS signals is proposed. The basic hypothesis test model is constructed

based on the features of environmental MPCs in received GNSS signals.

- 2) The concept of VA is used to build a geometric multipath propagation model of GNSS signals in urban canyons. The mirror images of the GNSS receiver induced by the environmental reflective surface are modeled as VAs to obtain a predicted baseline of environment MPCs at any time, according to the movement of satellites, which is a key factor in the basic hypothesis test model.
- 3) RIS is used to artificially improve the reflective environment and then enhance the detection performance of the proposed approach. We also provide an optimized RIS configuration to improve the quality of the targeted MPCs.
- 4) The performance of the proposed multipath-assisted passive detection approach is analyzed theoretically and validated by Monte Carlo simulations. Realistic simulation scenarios are also built using STK and ray tracing to evaluate the proposed approach.

The remainder of this paper is organized as follows. In Section II, we describe the received signal model of GNSS and the hypothesis testing scheme based on the signal model. Section III provides the basic decision rule and performance indicators of our hypothesis testing scheme in the target detection scenario. We propose a multipath-assisted detection method with learning and detection stages in Section IV to model the environment. In Section V, we introduce the RIS into the detection scheme and design a scheme to optimize the RIS configuration. Simulation results are presented in Section VI, followed by our conclusions in Section VII.

## II. PROBLEM FORMULATION

### A. Received Signal Model of GNSS

The basic model of GNSS signal is a modulated direct sequence spread spectrum signal with  $N_{PN}$ -bit Pseudo-Noise (PN) code, whose code chip duration is denoted by  $T_{PN}$ . Assuming  $P_t$  MPCs exist at time  $t$ , the received signal of the receiver ignoring thermal noise is

$$s(t) = \sum_{p=0}^{P_t-1} A_p D(t - \tau_p) C(t - \tau_p) \exp[j2\pi(f_c + f_p)t + j\theta_0], \quad (1)$$

where  $A_p$ ,  $\tau_p$ , and  $f_p$  are the complex amplitude, spatial propagation time delay, and Doppler shift of the  $p$ -th MPC, respectively;  $f_c$  is the carrier frequency; and  $\theta_0$  is the initial phase. For simplicity, we assume that the initial phase  $\theta_0$  of the signal is 0.  $D(t)$  and  $C(t)$  respectively denote the data sequence and the PN sequence. For GNSS signals, the length of the data chip far exceeds that of the PN chip; the data chip therefore does not change during the integration time, such that  $D(t) = 1$ .

At the receiver, we use the  $M$ -tap PMF to obtain the channel impulse response by correlating the demodulated signal with a local replica. The unified phase shift between adjacent taps is denoted as  $\Delta T/T_{PN}$ . Upon integrating the correlated signal

over the coherent integration period, we can derive the output of the  $m$ -th tap at epoch  $k$ :

$$\begin{aligned} r[k, m] &= \int_{t_k - T_{up}}^{t_k} s(t) s_{LO}(t, m) dt \\ &= \sum_{p=0}^{P_k-1} A_p[k] R_r[\tau_{p,k} - m\Delta T] \exp(j2\pi\Delta f_p k T_{up}) \end{aligned} \quad (2)$$

where  $s_{LO}$  is the local replica on the  $m$ -th tap.  $T_{up}$  is the update interval of the PMF.  $\Delta f_p$  is the residual Doppler frequency when the received GNSS signal is locked by the tracking loop. We only use the code phase for ToA estimation, which can be derived totally from the amplitude of correlation output. We assume the instant complex amplitude  $A_p[k]$  remains unchanged throughout integration.  $R_r(\cdot)$  is the auto-correlation function (ACF) of the PN code and

$$\begin{aligned} &R_r[\tau_{p,k} - m\Delta T] \\ &= \sum_{i=1}^{N-1} C(kT_{up} - iT_{PN} - \tau_{p,k}) C(-iT_{PN} - m\Delta T). \end{aligned} \quad (3)$$

It should be noted that the delay lock loop (DLL) and phase lock loop (PLL) are always used in a GNSS receiver for signal tracking. When the signal is locked, the code phase, Doppler frequency, and carrier phase of the local replica signal on a specific tap in the PMF are adjusted closely to the received signal, which can then be used as unbiased estimates of corresponding parameters of the received signal. On the other hand, as the ToA estimate can be obtained from the code phase, the resolution and accuracy of ToA are only affected by the output signal-to-noise ratio (SNR) of PMF [34].

### B. Target Detection Problem in Urban Canyons

We focus on target detection in complex urban environments and the identification of unexpected targets in supervised areas. GNSS is taken as the illuminator for passive detection. This scenario is illustrated in Fig. 1, where the arrow line indicates the propagation path. Fig. 1(a) shows a scenario where no target exists. The received signal primarily consists of the direct path component, environmental MPCs due to buildings and scattering. Fig. 1(b) shows a scenario where a target enters the detection field. The satellite signal interacts with the target, leading new MPCs to appear in the received signal as indicated by the red arrow line. In this case, except for the original direct path component and scattering, the received signal comprises two core elements: environmental MPCs and new induced MPCs from the target, which is denoted by targeted MPCs in Fig. 1.

Fig. 2 depicts variation in the received signal in the presence and absence of a target. The left figure presents a scenario without a target, where the received signal is simply represented as the LOS path and environmental MPCs (i.e., 1). The right figure depicts the received signal when a target is present; here, new targeted MPCs appear in the received signal. Target detection involves identifying targets that enter the detection field based on variation in the received signal.

For no-target scenario, the channel impulse response measurement on the  $m$ -th tap consists of two parts: environmental MPCs  $r[k, m]$  and measurement noise, represented as follows:

$$y[k, m] = r[k, m] + w[k, m], \quad (4)$$

where  $w[k, m]$  is measurement noise modeled by the additive complex Gaussian distribution with zero mean and a variance of  $\sigma_w^2$ .

If a target enters the detection field, then a new targeted MPC  $v[k, m]$  will appear in the received signal due to signal reflection and scattering from the target:

$$v[k, m] = \sum_{l=0}^{L_k-1} B_l[k] R_v[\tau_{l,k} - m\Delta T] \exp(j2\pi f_l k T_{up}), \quad (5)$$

where  $L_k$  is the number of new MPCs at epoch  $k$ .  $B_l$ ,  $\tau_{l,k}$ , and  $f_l$  denote the complex amplitude, time delay, and Doppler shift of the  $l$ -th targeted MPC, respectively.  $R_v[\tau_{l,k} - m\Delta T]$  is an ACF associated with new targeted MPCs, which has the same expression with (3).

The received signal includes three components (i.e., environmental MPCs, targeted MPCs, and noise):

$$y[k, m] = r[k, m] + v[k, m] + w[k, m]. \quad (6)$$

We consider the single-moment detection problem in this paper. For brevity, we omit the subscript  $k$  in the following description. We use vectors to represent elements in the received signal at the  $k$ -th epoch as follows:

$$\begin{aligned} \mathbf{y} &= [y(0), \dots, y(M-1)]^T, \mathbf{r} = [r(0), \dots, r(M-1)]^T, \\ \mathbf{v} &= [v(0), \dots, v(M-1)]^T, \mathbf{w} = [w(0), \dots, w(M-1)]^T. \end{aligned} \quad (7)$$

The MPCs contained in the received signal vary in both cases. Target detection can thus be described as a binary hypothesis test, where the null hypothesis  $\mathcal{H}_0$  indicates that no target exists in the detection field and the alternative hypothesis  $\mathcal{H}_1$  indicates that a target is present:

$$\begin{aligned} \mathcal{H}_0 : \mathbf{y} &= \mathbf{r} + \mathbf{w} \\ \mathcal{H}_1 : \mathbf{y} &= \mathbf{r} + \mathbf{v} + \mathbf{w}. \end{aligned} \quad (8)$$

The corresponding detection threshold is calculated according to hypothesis testing criteria; target detection is realized based on the testing results. Next, we present several detection methods and their performance analysis based on different assumptions.

According to the characteristic of GNSS signals, especially the modernized GNSS signals such as L1C or B1C, the spreading gain is large enough to provide adequate output SNR for a ground-based receiver. Moreover, a static receiver with fixed position is used as the detector in the proposed approach. Extremely long coherent integration time can be used to further improve the output SNR to meet the requirement to resolve the parameters of multipath signals. The impact of unresolved multipath is mitigated by super-resolution tracking algorithms [35], [36]. GNSS satellites are always in high speed motion, so the delay of each received multipath component is also in rapid variation. Sometimes two paths may fall into unresolved delay gap, but the overlap time is tolerable for

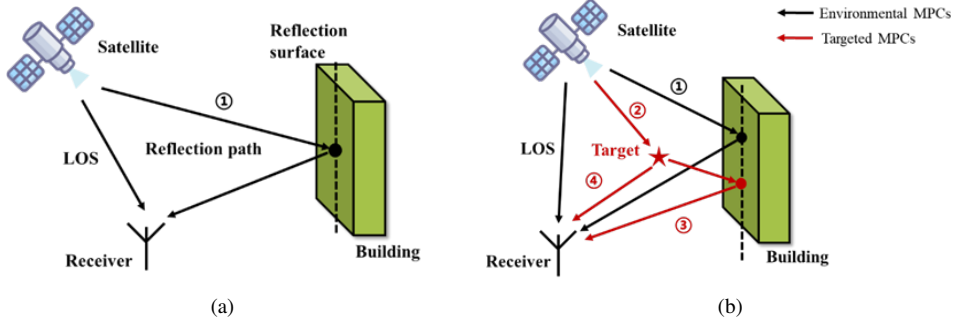


Fig. 1. The scenarios of target detection in urban canyon. (a) No target. (b) Targeted entry.

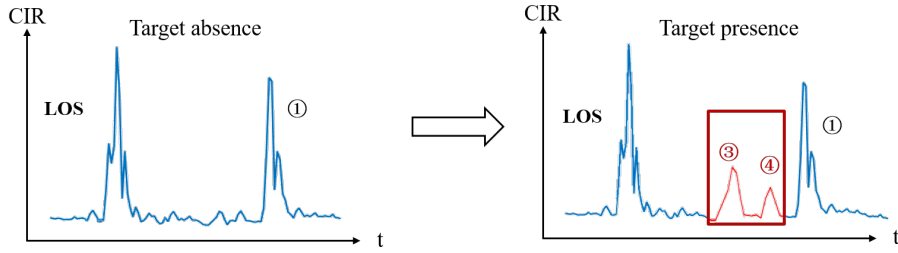


Fig. 2. The variation of the received signal waveform

super-resolution algorithms. So the accuracy of the estimated signal parameters can be guaranteed.

### III. BASIC DETECTION SCHEME

In this section, we provide the basic decision rule and performance analysis of our hypothesis testing scheme in the target detection scenario. We first give fundamental assumptions for the proposed scheme. Then we derive detection performance indicators, namely the detection probability and false alarm probability.

#### A. Fundamental Assumptions

The direct path is only related to the known position of the receiver and predictable positions of satellites, whose time delay can be accurately estimated. Hence, the LOS path does not interact with the environment and does not provide valid information for target detection. Based on the estimated time delay, we can identify whether a LOS component presents in the received signal and which path corresponds to the LOS component so that the LOS component can be removed during detection. Therefore, we neglect the present of LOS component and model the remaining multipath components as a complex Gaussian distribution. The distribution assumptions for each component of the received signal and its model parameters are introduced below.

**Assumption 1:** The noise of the  $m$ -th tap  $w[m]$  follows the zero-mean complex Gaussian distribution with variance  $\sigma_w^2$ :  $w[m] \sim \mathcal{CN}(0, \sigma_w^2)$ .

**Assumption 2:** Multipath signals' propagation paths are independent of each other. The amplitude of each MPC is independently and identically distributed in a complex Gaussian distribution with a mean of 0 and a variance  $\sigma_{MPC}^2$ ; that is,  $A_p, B_l \sim \mathcal{CN}(0, \sigma_{MPC}^2)$ .

**Assumption 3:** The receiver encounters many propagation paths from different directions in complex urban environments. Therefore,  $r[m]$  and  $v[m]$  obey the following distribution based on the central limit theorem [37], respectively:

$$r[m] \sim \mathcal{CN}\left(0, \sum_{p=0}^{P-1} \sigma_{MPC}^2 |R_r[\tau_p - m\Delta T]|^2\right), \quad (9)$$

$$v[m] \sim \mathcal{CN}\left(0, \sum_{l=0}^{L-1} \sigma_{MPC}^2 |R_v[\tau_l - m\Delta T]|^2\right). \quad (10)$$

#### B. Likelihood Ratio Test

Given the above assumptions, we can derive likelihood functions in our binary hypothesis test under assumptions. When no target appears in the detection field (i.e., under the null hypothesis  $\mathcal{H}_0$ ), the  $M$ -dimensional observation vector  $\mathbf{y}$  obeys the following distribution:

$$\mathbf{y} | \mathcal{H}_0 \sim \mathcal{CN}(0, \mathbf{C}_w), \quad \mathbf{C}_w = \sigma_{MPC}^2 \mathbf{R} \mathbf{R}^H + \sigma_w^2 \mathbf{I}_M, \quad (11)$$

where  $\mathbf{I}_M$  is an  $M$ -rank identity matrix.  $\mathbf{R}$  is composed of environmental MPC:

$$\mathbf{R} = [\mathbf{g}_0, \mathbf{g}_1, \dots, \mathbf{g}_{P-1}]_{M \times P}, \quad (12)$$

where

$$\begin{aligned} \mathbf{g}_p = & [A_p R[\tau_p - 0\Delta T] e^{j2\pi\Delta f_p T_{up}}, \\ & \dots, A_p R[\tau_p - (M-1)\Delta T] e^{j2\pi\Delta f_p T_{up}}]^T. \end{aligned} \quad (13)$$

Under the alternative hypothesis  $\mathcal{H}_1$ , targeted MPCs appear in the received signal and are distributed as

$$\mathbf{y} | \mathcal{H}_1 \sim \mathcal{CN}(0, \mathbf{C}_w + \mathbf{C}_v), \quad \mathbf{C}_v = \sigma_{MPC}^2 \mathbf{V} \mathbf{V}^H, \quad (14)$$

where  $\mathbf{V}$  is an  $M \times L$  matrix composed of targeted MPC similar to  $\mathbf{R}$ . When the environmental MPC in the received signal is estimated, we can derive  $\mathbf{C}_w$  based on (13). Further, we can estimate the targeted MPC in the received signal by removing the environmental MPC, and thus estimate  $\mathbf{C}_v$ , similar to the calculation of  $\mathbf{C}_w$ . Therefore, how to model the environment and predict the environmental MPC in the received signal at the detection moment is the core problem, which is solved in the following section. Here we only discuss theoretically the impact of these two covariance matrices on the detection performance.

Ultimately, the PDFs of the observation vector can be described as

$$p(\mathbf{y} | \mathcal{H}_0) = \frac{1}{\pi^M |\mathbf{C}_w|} \exp(-\mathbf{y}^H \mathbf{C}_w^{-1} \mathbf{y}), \quad (15)$$

$$p(\mathbf{y} | \mathcal{H}_1) = \frac{1}{\pi^M |\mathbf{C}_w + \mathbf{C}_v|} \exp\left[-\mathbf{y}^H (\mathbf{C}_w + \mathbf{C}_v)^{-1} \mathbf{y}\right], \quad (16)$$

The likelihood ratio is defined as

$$\Lambda(\mathbf{y}) = \frac{p(\mathbf{y} | \mathcal{H}_1)}{p(\mathbf{y} | \mathcal{H}_0)}. \quad (17)$$

Upon substituting (15) and (16) into (17), and after taking the logarithm of (17), we derive the following likelihood ratio under the basic scheme:

$$\begin{aligned} & \Lambda_{Basic}(\mathbf{y}) \\ &= \ln \frac{|\mathbf{C}_w|}{|(\mathbf{C}_w + \mathbf{C}_v)^{-1}|} + \mathbf{y}^H \left[ \mathbf{C}_w^{-1} - (\mathbf{C}_w + \mathbf{C}_v)^{-1} \right] \mathbf{y}. \end{aligned} \quad (18)$$

The test statistic is as follows once constants have been discarded:

$$\begin{aligned} T_{Basic}(\mathbf{y}) &= \mathbf{y}^H \left[ \mathbf{C}_w^{-1} - (\mathbf{C}_w + \mathbf{C}_v)^{-1} \right] \mathbf{y} \\ &= \mathbf{y}^H \mathbf{C}_w^{-1} \mathbf{C}_v (\mathbf{C}_v + \mathbf{C}_w)^{-1} \mathbf{y}. \end{aligned} \quad (19)$$

By setting a judgment threshold  $\gamma_{Basic}$ , we can write the decision criterion thusly: if  $T_{Basic}(\mathbf{y}) > \gamma_{Basic}$ , then an abnormal target exists in the detection field; if  $T_{Basic}(\mathbf{y}) \leq \gamma_{Basic}$ , then no target exists and detection will continue.

### C. Detection Performance Indicator

The PDF of the test statistic in the basic scheme will be given next, and its false alarm rate and detection probability will be derived theoretically as indicators of detection performance.

The matrices  $\mathbf{C}_w$  and  $\mathbf{C}_v$  are both positive semi-definite Hermitian matrices. We define  $\mathbf{x}$  as

$$\mathbf{x} = \mathbf{D}_B^H \Lambda_w^{-\frac{1}{2}} \mathbf{D}_w^H \mathbf{y}. \quad (20)$$

After linear transformation, the test statistic (19) can be rewritten as

$$T_{Basic}(\mathbf{x}) = \mathbf{x}^H \Lambda_B (\Lambda_B + \mathbf{I}_M)^{-1} \mathbf{x} = \sum_{m=0}^{M-1} \frac{\lambda_{B_m}}{\lambda_{B_m} + 1} |x[m]|^2 \quad (21)$$

where

$$\begin{aligned} \mathbf{B} &= \left( \mathbf{D}_w \sqrt{\Lambda_w}^{-1} \right)^H \mathbf{C}_v \mathbf{D}_w \sqrt{\Lambda_w}^{-1}, \\ \Lambda_B &= \text{diag}(\lambda_{B_0}, \lambda_{B_1}, \dots, \lambda_{B_{M-1}}), \\ \Lambda_w &= \text{diag}(\lambda_{w_0}, \lambda_{w_1}, \dots, \lambda_{w_{M-1}}). \end{aligned}$$

$\Lambda_B$  and  $\Lambda_w$  are composed of the eigenvalues of  $\mathbf{B}$  and  $\mathbf{C}_w$ .  $\mathbf{D}_B$  and  $\mathbf{D}_w$  denote the corresponding modal matrix.

Next, we use the false alarm rate and detection probability to evaluate detection performance. We note that  $|x[m]|^2$  is a proportional chi-square distributed variable with two degrees of freedom and that each random variable is independent. Consequently, the test statistic can be written as:

$$T_{Basic}(\mathbf{x}) = \sum_{m=0}^{M-1} \alpha_m \chi_2^2, \quad (22)$$

$$\text{where } \alpha_m = \begin{cases} \frac{\lambda_{B_m}}{2(\lambda_{B_m} + 1)}, & \mathcal{H}_0 \\ \frac{\lambda_{B_m}}{2}, & \mathcal{H}_1 \end{cases}.$$

**Lemma:** For  $y = \sum_m I_m x_m$ , if instances of  $I_m$  differ from each other and  $x_m$  follow the chi-square distribution  $\chi_2^2$ , then the PDF of  $y$  can be expressed as [38]

$$p(y) = \begin{cases} \sum_{m=0}^{M-1} \frac{C_m}{2I_m} \exp\left(-\frac{y}{2I_m}\right) & , y \leq 0 \\ 0 & , y < 0 \end{cases}, \quad (23)$$

$$\text{where } C_m = \prod_{\substack{i=0 \\ i \neq m}}^{M-1} \frac{1}{1 - I_i/I_m}.$$

We can use test statistic distributions at a threshold of  $\gamma_{Basic}$  to derive the detection probability  $P_{D-Basic}$  and the false alarm rate  $P_{FA-Basic}$ . The detailed derivation is described in Appendix A.

$$\begin{aligned} P_{FA-Basic} &= \Pr\{T_{Basic}(\mathbf{x}) > \gamma_{Basic} | \mathcal{H}_0\} \\ &= \int_{\gamma_{Basic}}^{+\infty} p(T_{Basic} | \mathcal{H}_0) dT_{Basic}, \\ &= \sum_{m=0}^{M-1} A_{m-Basic} \exp\left(-\frac{\gamma_{Basic}}{\alpha_m}\right) \end{aligned} \quad (24)$$

$$\begin{aligned} P_{D-Basic} &= \Pr\{T_{Basic}(\mathbf{x}) > \gamma_{Basic} | \mathcal{H}_1\} \\ &= \int_{\gamma_{Basic}}^{+\infty} p(T_{Basic} | \mathcal{H}_1) dT_{Basic}, \\ &= \sum_{m=0}^{M-1} B_{m-Basic} \exp\left(-\frac{\gamma_{Basic}}{\lambda_{B_m}}\right), \end{aligned} \quad (25)$$

$$\text{where } \alpha_m = \frac{\lambda_{B_m}}{2(\lambda_{B_m} + 1)}, \quad A_{m-Basic} = \prod_{\substack{i=0 \\ i \neq m}}^{M-1} \frac{1}{1 - \alpha_i/\alpha_m},$$

$$B_{m-Basic} = \prod_{\substack{i=0 \\ i \neq m}}^{M-1} \frac{1}{1 - \lambda_{B_i}/\lambda_{B_m}}.$$

The test statistic is a weighted sum of the chi-square random variable. Thus, the system's detection performance is related to the covariance matrix of the received signal and the noise variance. However, in complex urban environments, buildings and environmental scatterers generate substantial clutter in the

received signal. The MPCs produced from interaction with the target can be easily drowned in this clutter. Hence, identifying environmental MPCs is important in the proposed scheme.

#### IV. MULTIPATH-ASSISTED DETECTION

In this section, we use a multipath-assisted scheme to obtain accurate environmental MPC information. The concept of VA is used to equivalently describe the propagation path of reflected signals from NLOS to LOS. Then the detection entails two stages: an offline training stage and an online detection stage. In the first stage, we estimate the geographic distribution of VAs based on the received GNSS signals. In the second stage, we estimate environmental MPCs at the detection epoch based on the geometric relationship between VAs and the satellites. The modified detection performance indicators are also derived in analytical expression.

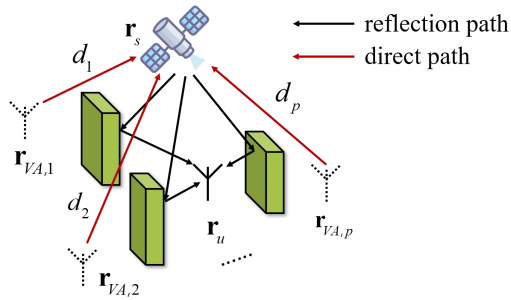


Fig. 3. The scenario of multipath-assisted scheme.

##### A. Estimation Error of Environmental MPC with Multipath Assistance

As displayed in Fig. 3, we take the mirror points of the static GNSS receiver according to environmental reflections as the VAs. Thus the reflective path serves as a direct path from the satellite to VAs. Next, as per geometrical optics theory, the propagation distance of a reflected MPC is

$$d_p = c\tau_p = \|\mathbf{r}_s - \mathbf{r}_{VA,p}\|, \quad (26)$$

where  $c$  is the speed of light, and  $\mathbf{r}_s = [x_s, y_s, z_s]^T$  is the satellite's position.  $\mathbf{r}_{VA,p} = [x_{VA,p}, y_{VA,p}, z_{VA,p}]^T$  is the VA's position corresponding to the  $p$ -th MPC. Therefore, VAs' positions and the propagation delay are coupled.

In the training phase (i.e., no target in the detection field), we first estimate VAs' positions using the received signal's time delay measurements. Each VA is equivalent to a virtual receiver with the same clock bias as the original receiver, and receives multiple GNSS signals reflected by the same reflecting surface. The data association is necessary to estimate VA's position, which is to determine the correspondence between VA and MPCs. Some effective Bayesian filters [16] have been developed to perform VA positioning and data association simultaneously. To reduce the computational load, we use a multipath tracking approach to estimate VA's position in this paper. The detailed description of the multipath tracking approach we used can be found in [35], [36]. When the data association is solved, the position of each VA can then be

estimated by an extended Kalman filter using received signals during a period. The diagram of VA is shown in Fig. 4. With the help of VAs, we can model environmental MPCs as deterministic signals to improve detection performance.

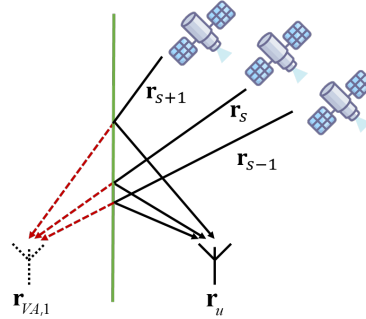


Fig. 4. The diagram of VA. The receiver is stable, receiving signals from moving satellites. The position of each VA can be estimated by an extended Kalman filter using received signals during a period.

In the detection stage, we use an estimated VA combined with the satellite's position calculated by the satellite ephemeris to estimate environmental MPCs. The VA model enables us to estimate the output of the  $m$ -th tap  $\hat{r}[m]$  at an epoch:

$$\hat{r}[m] = \sum_{p=0}^{P-1} \hat{A}_p(\hat{\tau}_p) \hat{R}(\hat{\tau}_p - m\Delta T), \quad (27)$$

where  $\hat{\tau}_p$  is the time delay estimated by the VA,  $\hat{A}_p(\hat{\tau}_p)$  is the estimated amplitude related to propagation loss, and  $\hat{R}(\hat{\tau}_p - m\Delta T)$  is the estimated ACF. Therefore, at any epoch, the environmental MPCs in vector form can be represented as

$$\hat{\mathbf{r}} = [\hat{r}[0], \hat{r}[1], \dots, \hat{r}[M-1]]^T. \quad (28)$$

Several assumptions are introduced in this section to better describe our extended scheme.

**Assumption 4:** The estimated position of the satellite  $\hat{\mathbf{r}}_s = [\hat{x}_s, \hat{y}_s, \hat{z}_s]^T$  is calculated by the ephemeris with a certain error [39]. Let  $\mathbf{e} = \hat{\mathbf{r}}_s - \mathbf{r}_s = [e_x, e_y, e_z]^T$  be the satellite position's estimation error.

**Assumption 5:** The estimated VA's position calculated by the received signal is defined as  $\hat{\mathbf{r}}_{VA,p} = [\hat{x}_{VA,p}, \hat{y}_{VA,p}, \hat{z}_{VA,p}]^T$ . The estimation error of the VA's position is defined as  $\delta_p = \hat{\mathbf{r}}_{VA,p} - \mathbf{r}_{VA,p} = [\delta_{p,x}, \delta_{p,y}, \delta_{p,z}]^T$ . For simplicity, the zero-mean Gaussian distribution is adopted, wherein  $\delta_p \sim \mathcal{CN}(0, \sigma_{VA}^2 \mathbf{I})$ .

##### B. Test Statistic

The test statistic of our multipath-assisted detection scheme is derived from the preceding assumptions. The VAs' positions are obtained during offline training. In the detection phase, the satellite's position can also be determined using the ephemeris. Environmental MPCs are therefore estimated based on the time delay between the satellite and VAs, and then can be removed from the received signal. The hypothesis test (8) is subsequently rewritten as

$$\begin{aligned} \mathcal{H}_0 : \mathbf{y} &= \xi + \mathbf{w}, \\ \mathcal{H}_1 : \mathbf{y} &= \mathbf{v} + \xi + \mathbf{w}, \end{aligned} \quad (29)$$

where  $\xi = \hat{\mathbf{r}} - \mathbf{r}$  is the estimation error of environmental MPCs due to the ephemeris and VA estimation error.

To obtain the PDF of an observation, the estimated time delay is represented as

$$\hat{\tau}_p = \frac{\|\hat{\mathbf{r}}_s - \hat{\mathbf{r}}_{VA,p}\|}{c} = \frac{\|(\mathbf{r}_s - \mathbf{r}_{VA,p}) + (\mathbf{e} - \delta_p)\|}{c}. \quad (30)$$

A function  $f_s$ , which computes the distance from the satellite, is defined by

$$f_s(x, y, z) = \sqrt{(x_s - x)^2 + (y_s - y)^2 + (z_s - z)^2}. \quad (31)$$

Then, the actual delay and estimated delay are calculated:

$$\tau_p = \frac{1}{c} \cdot f(x_{VA,p}, y_{VA,p}, z_{VA,p}), \quad (32)$$

$$\hat{\tau}_p = \frac{1}{c} \cdot f(x_{VA,p} + \Delta_x, y_{VA,p} + \Delta_y, z_{VA,p} + \Delta_z), \quad (33)$$

where  $\Delta_{VA,p}$  is the superposition of the VA estimation error and ephemeris error, expressed as

$$\Delta_{VA,p} = [\Delta_x, \Delta_y, \Delta_z]^T = [\delta_{p,x} - e_x, \delta_{p,y} - e_y, \delta_{p,z} - e_z]^T. \quad (34)$$

Based on Assumptions 4 and 5, the distribution is obtained by

$$\Delta_{VA,p} \sim \mathcal{CN}(\mathbf{e}, \sigma_{VA}^2 \mathbf{I}). \quad (35)$$

The time delay difference is represented as  $\delta_{\tau,p} = \hat{\tau}_p - \tau_p$ , which can be approximated using a linear term as

$$\delta_{\tau,p} \sim \frac{\mathbf{A}_p^T \Delta_{VA,p}}{c}, \quad (36)$$

where  $\mathbf{A}_p = [A_{1,p}, A_{2,p}, A_{3,p}]^T$  is the coefficient given by

$$A_{1,p} = \frac{\partial f}{\partial x} \Big|_{\mathbf{r}=\mathbf{r}_{VA,p}}, A_{2,p} = \frac{\partial f}{\partial y} \Big|_{\mathbf{r}=\mathbf{r}_{VA,p}}, A_{3,p} = \frac{\partial f}{\partial z} \Big|_{\mathbf{r}=\mathbf{r}_{VA,p}} \quad (37)$$

Based on (35) - (37), we get:

$$\mathbf{A}_p^T \Delta_{VA,p} \sim \mathcal{CN}\left(\mathbf{A}^T \mathbf{e}, \sigma_{VA}^2 |\mathbf{A}_p|^2\right). \quad (38)$$

Then, we can obtain the following distribution of the time delay error:

$$\begin{aligned} \delta_{\tau,p} &\sim \mathcal{CN}(u_{\tau,p}, \sigma_{\tau,p}^2), \\ u_{\tau,p} &= \frac{\mathbf{A}_p^T \mathbf{e}}{c}, \sigma_{\tau,p}^2 = \frac{\sigma_{VA}^2 \|\mathbf{A}_p\|^2}{c^2}. \end{aligned} \quad (39)$$

The error of estimated environmental MPCs at the  $m$ -th tap is represented as

$$\begin{aligned} \xi(m) &= \hat{r}(m) - |r(m)| \\ &= \sum_{p=0}^{P-1} \left[ \hat{A}_p(\hat{\tau}_p) \hat{R}(\hat{\tau}_p - m\Delta T) - A_p(\tau_p) R(\tau_p - m\Delta T) \right]. \end{aligned} \quad (40)$$

In addressing satellite-to-ground path loss, the path loss is given by [40]

$$PL(\tau, \theta) = FSPL(\tau, f) + L_A(f, \theta) + \eta(\theta), \quad (41)$$

where  $\theta$  is the elevation angle, referring to the angle formed between the horizon and the line to the satellite.  $f$  is the carrier frequency.  $L_A(f, \theta)$  represents attenuation due to atmospheric

absorption.  $\eta(\theta)$  denotes excess path loss due to interactions with near-surface urban structures.  $FSPL(\tau, f)$  is the free space path loss expressed as

$$FSPL(\tau, f) = 20\log(f) + 20\log(c \cdot \tau) - 147.55. \quad (42)$$

Normally, the PN sequences used for time-of-arrival measurement have excellent auto-correlation characteristics. The ACF value drops rapidly when the delay between two sequences exceeds 1 chip. We consider the BPSK modulation of the GNSS signal, which can be extended simply to modernized modulations of GNSS. (3) can then be approximately rewritten as

$$R(\tau_p) \approx \begin{cases} N_{PN} \left( 1 - \frac{1}{T_{PN}} |\tau_p| \right); & |\tau_p| \leq T_{PN}, \\ 0; & |\tau_p| > T_{PN}. \end{cases} \quad (43)$$

The satellite transmit power is denoted by  $P_t$ . Based on (41) and (43), (40) can be rewritten as

$$\begin{aligned} \xi(m) &= \sum_{p=0}^{P-1} \left\{ 20 \cdot \frac{N_{PN}}{T_{PN}} [\hat{\tau}_p \log(c \hat{\tau}_p) - \tau_p \log(c \tau_p)] \right. \\ &\quad \left. + 20N_{PN} \log\left(\frac{\tau_p}{\hat{\tau}_p}\right) + [L_A(f, \theta) + \eta(\theta) - P_t] \cdot \frac{N_{PN}}{T_{PN}} \cdot \delta_{\tau,p} \right\}. \end{aligned} \quad (44)$$

We define the function  $g(x)$  as  $g(x) = x \log(c \cdot x)$ , after which

$$\begin{aligned} \hat{\tau}_p \log(c \cdot \hat{\tau}_p) - \tau_p \log(c \cdot \tau_p) &= g(\hat{\tau}_p) - g(\tau_p) \\ &= g(\tau_p + \delta_{\tau,p}) - g(\tau_p) \\ &\sim \frac{\partial g}{\partial x} \Big|_{x=\tau_p} \delta_{\tau,p} \end{aligned} \quad (45)$$

Because the error  $\delta_{\tau,p}$  is small,  $\log(\tau_p/\hat{\tau}_p) \approx 0$ . The propagation distance is also much larger than the position error. We consider true VAs and estimated VAs to have the same elevation angle. We can therefore determine that

$$\begin{aligned} \xi(m) &\sim \sum_{p=0}^{P-1} \left\{ \left[ 20 \frac{\partial g}{\partial x} \Big|_{x=\tau_p} + L_A(f, \theta) + \eta(\theta) - P_t \right] \right. \\ &\quad \times \left. \frac{N_{PN}}{T_{PN}} \cdot \delta_{\tau,p} \right\}. \end{aligned} \quad (46)$$

Based on (39), the distribution of environmental MPCs' error can be derived as

$$\begin{aligned} \xi(m) &\sim \mathcal{CN}(u_\delta, \sigma_\delta^2), \\ u_\delta &= \sum_{p=0}^{P-1} \frac{P_{\delta,p} \mathbf{A}_p^T \mathbf{e}}{c}, \sigma_\delta^2 = \sum_{p=0}^{P-1} \left( \frac{P_{\delta,p} \sigma_{VA}}{c} \right)^2 \|\mathbf{A}_p\|^2, \end{aligned} \quad (47)$$

where

$$P_{\delta,p} = \left[ 20 \cdot \frac{\partial g}{\partial x} \Big|_{x=\tau_p} + L_A(f, \theta) + \eta(\theta) - P_t \right] \cdot \frac{N_{PN}}{T_{PN}}. \quad (48)$$

We can identify the likelihood function based on the above analysis of estimation error. Under the null hypothesis, the observation vector abides by the following distribution:

$$p(\mathbf{y} | \mathcal{H}_0) = \frac{1}{\pi^M (\sigma_w^2 + \sigma_\delta^2)^M} \exp \left[ -\frac{(\mathbf{y} - \mathbf{u}_\delta)^H (\mathbf{y} - \mathbf{u}_\delta)}{\sigma_w^2 + \sigma_\delta^2} \right]. \quad (49)$$

Under the alternative hypothesis, the distribution is:

$$p(\mathbf{y} | \mathcal{H}_1) = \frac{1}{\pi^M |\mathbf{C}_{VA}|} \exp \left[ -(\mathbf{y} - \mathbf{u}_\delta)^H \mathbf{C}_{VA}^{-1} (\mathbf{y} - \mathbf{u}_\delta) \right], \quad (50)$$

where

$$\mathbf{C}_{VA} = \mathbf{C}_v + (\sigma_w^2 + \sigma_\delta^2) \mathbf{I}_M. \quad (51)$$

Since the receiver position and the environment do not change, we can obtain the covariance matrices by learning the environmental information and then predicting the environmental MPC in the received signal at the detection moment. We can determine which part of the received signal corresponds to the environmental MPCs according to the time delay of the environmental MPCs estimated by VA's and satellites' positions at each detection moment. The remaining part of the received signal is the multipath component caused by the target, which is used to calculate  $\mathbf{C}_v$ .  $\sigma_w^2$  is related to the scatter and receiver performance.  $\sigma_\delta^2$  is calculated by (47). By the above process, we can then calculate the covariance matrix  $\mathbf{C}_{VA}$ .

Upon substituting (49) and (50) into (17), and after taking the logarithm, the likelihood ratio of the multipath-assisted detection scheme is calculated as shown in (52). Based on the matrix inversion lemma [41], the inversion matrix  $\mathbf{C}_{VA}^{-1}$  is derived as

$$\begin{aligned} \mathbf{C}_{VA}^{-1} &= [\mathbf{C}_v + (\sigma_w^2 + \sigma_\delta^2) \mathbf{I}_M]^{-1} \\ &= \frac{1}{\sigma_w^2 + \sigma_\delta^2} \mathbf{I}_M - \mathbf{C}_v [\mathbf{C}_v + (\sigma_w^2 + \sigma_\delta^2) \mathbf{I}_M]^{-1}. \end{aligned} \quad (53)$$

The likelihood ratio (17) is rewritten as

$$\begin{aligned} \Lambda_{VA}(\mathbf{y}) &= \ln \frac{(\sigma_w^2 + \sigma_\delta^2)^M}{|\mathbf{C}_{VA}|} + \frac{1}{\sigma_w^2 + \sigma_\delta^2} (\mathbf{y} - \mathbf{u}_\delta)^H \\ &\quad \times \mathbf{C}_v [\mathbf{C}_v + (\sigma_w^2 + \sigma_\delta^2) \mathbf{I}_M]^{-1} (\mathbf{y} - \mathbf{u}_\delta). \end{aligned} \quad (54)$$

Upon adding the constant term to the threshold and multiplying by the scale factor  $\sigma_w^2 + \sigma_\delta^2$ , the test statistic  $T_{VA}(\mathbf{y})$  is

$$T_{VA}(\mathbf{y}) = (\mathbf{y} - \mathbf{u}_\delta)^H \mathbf{C}_v [\mathbf{C}_v + (\sigma_w^2 + \sigma_\delta^2) \mathbf{I}_M]^{-1} (\mathbf{y} - \mathbf{u}_\delta). \quad (55)$$

### C. Performance Analysis

As with the baseline scheme, we can discern the performance of our proposed multipath-assisted detection scheme. First, the test statistic in (55) can be rewritten after linear transformation as follows:

$$\begin{aligned} T_{VA}(\mathbf{x}) &= \mathbf{x}^H \mathbf{\Lambda}_v [\mathbf{\Lambda}_v + (\sigma_w^2 + \sigma_\delta^2) \mathbf{I}_M] \mathbf{x} \\ &= \sum_{m=0}^{M-1} \frac{\lambda_{v_m}}{\lambda_{v_m} + \sigma_w^2 + \sigma_\delta^2} |x[m]|^2, \end{aligned} \quad (56)$$

where  $\mathbf{x} = \mathbf{D}_v^H (\mathbf{y} - \mathbf{u}_\delta)$ .  $\mathbf{\Lambda}_v = \text{diag}(\lambda_{v_0}, \lambda_{v_1}, \dots, \lambda_{v_{M-1}})$ ,  $m = 0, \dots, M-1$  is composed of the eigenvalues of matrix  $\mathbf{C}_v$ .  $\mathbf{D}_v$  is the corresponding modal matrix. The test statistic therefore obeys the following distribution:

$$T_{VA}(\mathbf{x}) \sim \sum_{m=0}^{M-1} \beta_m \chi_2^2, \quad (57)$$

where  $\beta_m = \begin{cases} \frac{\lambda_{v_m} (\sigma_w^2 + \sigma_\delta^2)}{2(\lambda_{v_m} + \sigma_w^2 + \sigma_\delta^2)} & , \mathcal{H}_0 \\ \frac{\lambda_{v_m}}{2} & , \mathcal{H}_1 \end{cases}$ . Then, the false alarm rate is given as follows

$$P_{FA-VA} = \sum_{m=0}^{M-1} A_{m-VA} \cdot \exp \left( -\frac{\gamma_{VA}}{\beta_m} \right), \quad (58)$$

where  $\beta_m = \frac{\lambda_{v_m} (\sigma_w^2 + \sigma_\delta^2)}{2(\lambda_{v_m} + \sigma_w^2 + \sigma_\delta^2)}$ , and  $\gamma_{VA}$  is the judgment threshold calculated by the given false alarm rate. Next, the detection probability is as follows:

$$P_{D-VA} = \sum_{m=0}^{M-1} B_{m-VA} \cdot \exp \left( -\frac{\gamma_{VA}}{\lambda_{v_m}} \right), \quad (59)$$

where

$$A_{m-VA} = \prod_{\substack{i=0 \\ i \neq m}}^{M-1} \frac{1}{1 - \beta_i / \beta_m}, B_{m-VA} = \prod_{\substack{i=0 \\ i \neq m}}^{M-1} \frac{1}{1 - \lambda_{v_i} / \lambda_{v_m}}.$$

The derivation of the test statistic  $T_{VA}(\mathbf{x})$ , the false alarm rate  $P_{FA-VA}$ , and the detection probability  $P_{D-VA}$  are described in Appendix B.

In the advanced scheme, we use multipath-assisted detection to bolster system performance. First, the VA's position is obtained via offline training, giving a priori information for detection. Environmental MPCs are then estimated to lessen the impact of clutter on detection. Finally, we notice that the detection performance is mainly related to estimation error and noise variance, with a performance improvement compared with the basic scheme.

## V. RIS-ASSISTED DETECTION

The quality of the naturally reflected signals is often poor due to the attenuation. The performance of the proposed multipath-assisted detection scheme is heavily decided by the conditions of environment. To enhance the practicability of the proposed scheme, we introduce RIS to artificially rebuild the reflective environment. Furthermore, we also optimize the RIS configuration to further improve the target echo signal power after eliminating clutter and then strengthen detection performance in the dense urban environment.

### A. Target Detection Based on RIS-assisted Estimation of VA's Position

By introducing RISs, we can acquire VAs' positions via the geometric method as seen in Fig. 4. We first set a world coordinate system according to the right-hand rule, where the X-Y plane is the horizontal plane, and the z-axis is perpendicular to the X-Y plane and points to the sky. Physical reflective surfaces in the environment are replaced with RISs with known positions. VA's position is related to the orientation of RIS. Without loss of generality, we set RIS to lie in a plane parallel to the Y-Z plane, which matches the architectural characteristics of city buildings. We consider a stationary receiver with known position  $\mathbf{r}_u = [x_u, y_u, z_u]^T$ .

$$\Lambda_{VA}(\mathbf{y}) = \ln \frac{(\sigma_w^2 + \sigma_\delta^2)^M}{|\mathbf{C}_{VA}|} + (\mathbf{y} - \mathbf{u}_\delta)^H \left( -\mathbf{C}_{VA}^{-1} + \frac{1}{\sigma_w^2 + \sigma_\delta^2} \mathbf{I}_M \right) (\mathbf{y} - \mathbf{u}_\delta). \quad (52)$$

We assume the coordinate of the center of the  $p$ -th RIS is  $\mathbf{r}_{RIS,p} = [x_{RIS,p}, y_{RIS,p}, z_{RIS,p}]^T$ . The  $p$ -th VA is the mirror point of the receiver with respect to the  $p$ -th RIS. Since RIS is perpendicular to the X-Y plane, VA and receiver are in the same horizontal plane. The x-coordinate of VA is determined by the x-coordinates of RIS and receiver, i.e.,  $2x_{RIS,p} - x_u$ , so the position of the  $p$ -th VA is

$$\mathbf{r}_{VA,p} = [2x_{RIS,p} - x_u, y_u, z_u]^T. \quad (60)$$

If RIS is deployed in another plane, VA's position can be solved by a similar geometric method.

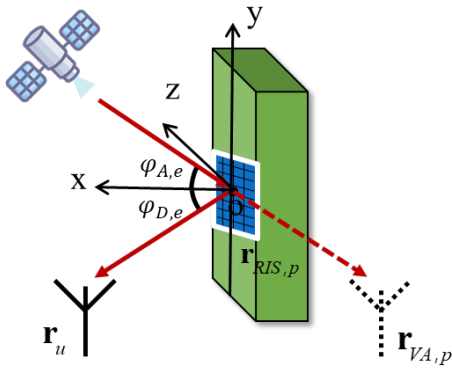


Fig. 5. Acquisition of VA positions by RIS.

Before deriving the test statistic, the assumptions underlying this scheme are given as follows.

**Assumption 6:** The receiver's position is obtained with no error; that is,  $\mathbf{r}_u$  is the receiver's true position.

To account for small errors in RIS positions, let  $\delta_{RIS} = \hat{\mathbf{r}}_{RIS,p} - \mathbf{r}_{RIS,p}$  be the RIS measurement error. Assumption 5 can then be replaced by Assumption 7.

**Assumption 7:** The estimation error of a VA's position,  $\delta_p = 2\delta_{RIS}$ , is the determination value derived from the RIS measurement error.

Based on the above assumptions, the time delay error (36) can be rewritten as

$$\delta_{\tau,p} = \frac{\mathbf{A}_p^T \Delta_{RIS,p}}{c}, \quad (61)$$

where  $\Delta_{RIS,p} = 2\delta_{RIS} - \mathbf{e}$ . Next, the error of estimated environmental MPCs is

$$\xi(m) = \sum_{p=0}^{P-1} \frac{P_{\delta,p} \mathbf{A}_p^T \Delta_{RIS,p}}{c}. \quad (62)$$

Then, the PDFs of the observation vector in (49) are rewritten for the RIS-assisted detection scheme as:

$$p(\mathbf{y} | \mathcal{H}_0) = \frac{1}{\pi^M \sigma_w^{2M}} \exp \left[ -\frac{(\mathbf{y} - \xi)^H (\mathbf{y} - \xi)}{\sigma_w^2} \right], \quad (63)$$

$$p(\mathbf{y} | \mathcal{H}_1) = \frac{1}{\pi^M |\mathbf{C}_{RIS}|} \exp \left[ -(\mathbf{y} - \xi)^H \mathbf{C}_{RIS}^{-1} (\mathbf{y} - \xi) \right], \quad (64)$$

where  $\mathbf{C}_{RIS} = \mathbf{C}_v + \sigma_w^2 \mathbf{I}_M$ . The covariance matrix calculation is similar to the calculation process in Section IV-B. We also estimate VAs' positions first and then use the VAs' positions to distinguish multipath MPCs and target MPCs in the received signal. Therefore  $\mathbf{C}_v$  can be calculated similarly by the calculation process described in Section IV-B. However, the introduction of RIS changes the error model of VA. The estimation error of VA is no longer a complex Gaussian distribution but a systematic fixed bias caused by the combination of RIS measurement error, ephemeris error, and path loss. Therefore,  $\sigma_\delta^2 = 0$  here.

The test statistic in the RIS-assisted detection scheme can finally be determined after calculating the log-likelihood ratio and adding the constant term to the threshold:

$$T_{RIS}(\mathbf{y}) = (\mathbf{y} - \xi)^H (\mathbf{C}_v + \sigma_w^2 \mathbf{I}_M)^{-1} (\mathbf{y} - \xi). \quad (65)$$

We can determine the performance of the RIS-assisted detection scheme in a similar fashion. First, the distribution of the test statistic is as follows:

$$T_{RIS}(\mathbf{x}) = \mathbf{x}^H \Lambda_v (\Lambda_v + \sigma_w^2 \mathbf{I}_M) \mathbf{x} = \sum_{m=0}^{M-1} \frac{\lambda_{v_m}}{\lambda_{v_m} + \sigma_w^2} |x[m]|^2, \quad (66)$$

where  $\mathbf{x} = \mathbf{D}_v^H (\mathbf{y} - \xi)$ . This test statistic therefore obeys the following distribution:

$$T_{RIS}(\mathbf{x}) \sim \sum_{m=0}^{M-1} \eta_m \chi_2^2, \quad (67)$$

where  $\eta_m = \begin{cases} \frac{\lambda_{v_m} \sigma_w^2}{2(\lambda_{v_m} + \sigma_w^2)}, & \mathcal{H}_0 \\ \frac{\lambda_{v_m}}{2}, & \mathcal{H}_1 \end{cases}$ . The false alarm rate is given as

$$P_{FA-RIS} = \sum_{m=0}^{M-1} A_{m-RIS} \exp \left( -\frac{\gamma_{RIS}}{\eta_m} \right), \quad (68)$$

where  $\eta_m = \frac{\lambda_{v_m} \sigma_w^2}{2(\lambda_{v_m} + \sigma_w^2)}$ , and  $\gamma_{RIS}$  is the judgment threshold calculated using the given false alarm rate. Next, the detection probability is

$$P_{D-RIS} = \sum_{m=0}^{M-1} B_{m-RIS} \exp \left( -\frac{\gamma_{RIS}}{\lambda_{v_m}} \right), \quad (69)$$

where

$$A_{m-RIS} = \prod_{i=0, i \neq m}^{M-1} \frac{1}{1 - \eta_i / \eta_m}, B_{m-RIS} = \prod_{i=0, i \neq m}^{M-1} \frac{1}{1 - \lambda_{v_i} / \lambda_{v_m}}.$$

The derivation of the test statistic  $T_{RIS}(\mathbf{x})$ , the false alarm rate  $P_{FA-RIS}$ , and the detection probability  $P_{D-RIS}$  are described in Appendix A-B.

## B. RIS Configuration to Optimize the Target Echo Signal

In urban canyons, the satellite signal reaches the ground with low power after multiple reflections, affecting detection performance. In this part, we optimize the target echo signal by designing the phase shift matrix of the passive RIS array to enhance received signal power.

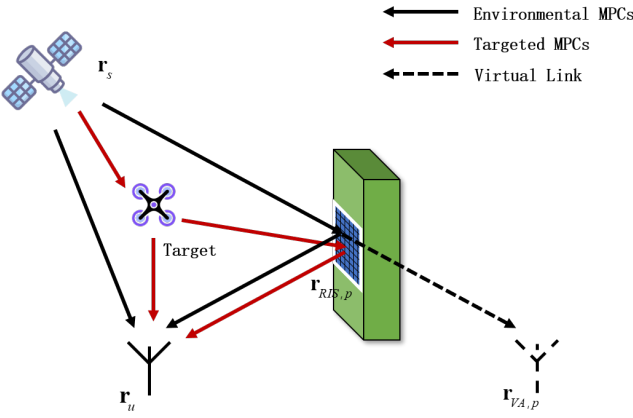


Fig. 6. Signal transmission channel model in RIS-assisted scenario

1) *System Geometry*: The signal propagation model in the RIS-assisted detection scenario is shown in Fig. 6. There are two types of target multipath signals. One is a direct echo signal transmitted directly from the target to the receiver, i.e., target - receiver. The other is the reflected echo signal reflected by a RIS and then reaching the receiver, i.e., target - RIS - receiver.

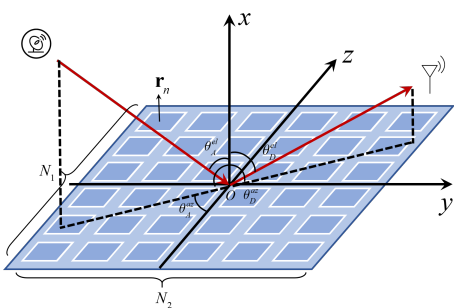


Fig. 7. Diagram of RIS in Cartesian coordinate.

The diagram of the RIS is shown in Fig. 7. Each RIS contains  $N_R = N_1 \times N_2$  mutually independent reflection units, where  $N_1$  and  $N_2$  are the number of rows and columns of the array, respectively. Without loss of generality, we assume that the RIS is laid in the Y-Z plane of the global coordinate system. Other poses of the RIS can be obtained by translation and rotation. The position coordinate of the reflection unit is  $\mathbf{r}_n = [0, z_{n,2}, z_{n,3}]^T$ , depending on the spacing of RIS unit. The Angle of arrival (AoA) from the target to the RIS and the Angle of departure (AoD) from the RIS to the receiver are denoted as  $\varphi_A$  and  $\varphi_D$ , respectively.  $\varphi_Q = [\theta_Q^{az}, \theta_Q^{el}]^T$ ,  $Q \in (A, D)$ , where  $\theta_Q^{az}, \theta_Q^{el}$  denotes the azimuth and elevation

angle. The local direction vector is defined as  $\mathbf{t}(\varphi_Q)$ , which is expressed as:

$$\mathbf{t}(\varphi_Q) = \begin{bmatrix} \cos(\theta_Q^{az}) \sin(\theta_Q^{el}) \\ \sin(\theta_Q^{az}) \sin(\theta_Q^{el}) \\ \cos(\theta_Q^{el}) \end{bmatrix}. \quad (70)$$

2) *Design of RIS Configuration*: The received signal at time  $t$  consisting the direct echo signal and the reflected echo signal can be expressed as:

$$y(t) = \left( \frac{\sqrt{K_r}}{\sqrt{K_r + 1}} h_d + \sum_{p=1}^{P-1} \frac{1}{\sqrt{K_r + 1}} \mathbf{H}_{r,p} \right) \sqrt{P_s} x(t) + w(t), \quad (71)$$

where  $h_d$  and  $\mathbf{H}_{r,p}$  represent the channel gains of direct echo signal and the reflected echo signal, respectively.  $P$  represents the number of propagation paths.  $K_r$  is the Rice factor.  $P_s$  is the satellite signal power reaching the ground.  $w(t)$  represents white Gaussian noise with zero mean and variance  $\sigma_w^2$ .

The direct echo channel gain is modeled as:

$$h_d = \alpha_d \exp(-j\phi_d), \quad (72)$$

where  $\lambda$  is the carrier wavelength.  $\sigma$  is the reflection cross section (RCS) of the target.  $\alpha_d$  and  $\phi_d$  represent the amplitude and phase of the direct echo signal respectively, which are calculated by:

$$\alpha_d = \sqrt{\frac{\lambda^2 \sigma}{16\pi^2 d_{TU}^2}}, \phi_d = \frac{2\pi f_c d_{TU}}{c},$$

where  $d_{TU}$  represents the distance from the target to the receiver.

The reflected echo channel gain is modeled as:

$$\mathbf{H}_{r,p} = \alpha_r \mathbf{a}^T(\varphi_{D,p}) \Omega_p \mathbf{a}(\varphi_{A,p}) \exp(-j\phi_{r,p}), \quad (73)$$

where  $\alpha_r$ ,  $\phi_r$  represent the amplitude and phase of the reflected echo signal calculated by:

$$\alpha_r = \sqrt{\frac{\lambda^2 \sigma}{64\pi^3 d_{TR,p}^2 d_{RU,p}^2}}, \phi_r = \frac{2\pi f_c (d_{TR,p} + d_{RU,p})}{c},$$

where  $d_{TR,p}$  and  $d_{RU,p}$  are the distance from the target to the RIS array and the distance from the RIS array to the receiver.  $\Omega_p$  represents the phase shift matrix of the RIS array, which is expressed as:

$$\Omega_p = \text{diag}(\omega_p) \in C^{N_R \times N_R} \omega_p = [\omega_{p,1}, \dots, \omega_{p,n}, \dots, \omega_{p,N_R}] \quad (74)$$

where  $\omega_p$  is the vector containing information of the amplitude and phase coefficients of the RIS reflection unit, and  $\omega_{p,n} = \beta_{p,n} e^{j\psi_{p,n}}$ ,  $\forall n = 1, 2, \dots, N_R$ .  $\beta_{p,n} \in (0, 1]$ ,  $\psi_{p,n} \in [0, 2\pi]$  denote the amplitude and phase of the reflection unit, respectively.  $\mathbf{a}(\cdot)$  is the steering vector of the RIS array, which can be obtained as:

$$\mathbf{a}(\varphi_Q) = [a_1(\varphi_Q), \dots, a_n(\varphi_Q), \dots, a_{N_R}(\varphi_Q)]^T$$

$$a_n(\varphi_Q) = \exp \left\{ j \frac{2\pi f_c}{c} [\mathbf{r}_n^T \mathbf{t}(\varphi_Q)] \right\}, \quad (75)$$

where  $\mathbf{r}_n$  is the position of the RIS reflection unit, the direction vector  $\mathbf{t}(\varphi_Q)$  is given by (70).

Substituting the above two channel gains into (71), we obtain:

$$y(t) = \left\{ \sum_{p=1}^{P-1} \frac{\alpha_{r,p}}{\sqrt{K_r + 1}} \mathbf{a}^T (\varphi_{D,p}) \Omega_p \mathbf{a} (\varphi_{A,p}) \exp(-j\phi_{r,p}) + \frac{\alpha_d \sqrt{K_r}}{\sqrt{K_r + 1}} \exp(-j\phi_d) \right\} \sqrt{P_s} x(t) + w(t) \quad (76)$$

We can maximize the received SNR by adjusting the phase of the RIS array to increase the signal power. The amplitude of each reflection unit in the RIS array is set to 1. The optimization problem can be formulated as follows:

$$\begin{aligned} & \max_{\Omega_p} \frac{P_r}{\sigma_w^2}, \\ & \text{s.t. } |\omega_{p,n}| = 1, \forall n = 1, \dots, N_R, \end{aligned} \quad (77)$$

where  $P_r$  represents the average echo signal power. Since the satellite signal is transmitted with a constant power,  $P_r$  can be calculated by

$$\begin{aligned} P_r &= \frac{1}{2T} \int_{t_0-T}^{t_0+T} |y(t) - w(t)|^2 dt \\ &= P_s \left| \frac{\alpha_d \sqrt{K_r}}{\sqrt{K_r + 1}} \exp(-j\phi_d) + \sum_{p=1}^{P-1} \frac{\alpha_{r,p}}{\sqrt{K_r + 1}} \mathbf{a}^T (\varphi_{D,p}) \Omega_p \mathbf{a} (\varphi_{A,p}) \exp(-j\phi_{r,p}) \right|^2. \end{aligned} \quad (78)$$

According to (74) - (76), we can rewritten the phase of RIS as

$$\mathbf{a}^T (\varphi_{D,p}) \Omega_p \mathbf{a} (\varphi_{A,p}) = \sum_{n=1}^{N_R} \exp[j\phi_{DA,p}(n) + j\psi_{p,n}], \quad (79)$$

where  $\phi_{DA,p} = \frac{2\pi f_c}{c} \mathbf{r}_n^T [\mathbf{t}(\varphi_{D,p}) + \mathbf{t}(\varphi_{A,p})]$  denotes the phase caused by the RIS steering vector and  $\psi_{p,n}$  denotes the adjustable RIS array phase shift.

Substituting (78) and (79) into (77), (77) can be rewritten as (80). Although constraint is nonconvex, the closed-form optimal solution can be derived according to the phase alignment principle [42]. Specifically, the objective function in (80) has the inequality relation as shown in (81). The inequality can take its maximum value only if all terms have the same phase. Thus, the target echo power takes the maximum value when the RIS phase shift satisfies the following conditions:

$$\begin{aligned} \psi_{p,n} &= \phi_{r,p} - \phi_d - \phi_{DA,p}(n) \\ &= \frac{2\pi f_c}{c} \{ [d_{TR,p} + d_{RU,p} - d_{TU}] - \mathbf{r}_n^T [\mathbf{t}(\varphi_{D,p}) + \mathbf{t}(\varphi_{A,p})] \}. \end{aligned} \quad (82)$$

Hence, the maximum target echo power is:

$$P_r = P_s \left( \frac{\alpha_d \sqrt{K_r}}{\sqrt{K_r + 1}} + N_R \sum_{p=1}^{P-1} \frac{\alpha_{r,p}}{\sqrt{K_r + 1}} \right)^2. \quad (83)$$

Therefore, with a fixed transmit signal, RIS can be used to compensate for power loss over long distances and provide high-quality reflection paths. If we can know the target's approximate location through other sensors or we want to

supervise a fixed area, we can design the corresponding RIS array phase shift matrix to maximize the target echo signal by the above method. In practice, it is a little tricky to obtain the accurate position of the detected target. Hence, we can divide the supervised area into many grids and give the a priori information about the probability of the target's appearance in the form of a determined distribution at each grid, e.g.,  $\mathbf{r}_t \sim \mathcal{N}(\bar{\mathbf{r}}_t, \sum r_t)$ . In this case, we can enhance the target echoes by assigning different duration to different phase shift modes according to the appearance probability in each grid.

## VI. SIMULATIONS RESULTS

In this section, we present numerical results to assess the detection performance of the basic detection scheme and its two variants, i.e., multipath-assisted and RIS-assisted detection schemes. Monte Carlo simulations are performed. The number of simulations is set as 5000. We first give the tolerable false alarm probability and calculate the judgment threshold based on it. Observation vectors are randomly generated for target detection. Then, we calculate the three schemes' test statistics for comparison with the corresponding detection thresholds. Finally, we compute the detection probability to evaluate system performance.

### A. Performance of Basic Detection Scheme

We first consider the effects of SNR and the number of available MPC on the detection probability  $P_D$  for the basic detection scheme.

Fig. 8 indicates the detection probability versus the SNR and propagation paths for the basic scheme. As shown in Fig. 8(a), the detection probability increases with SNR and then converges to 1. Besides, improving the requirement of the false alarm will reduce the detection performance. Then, we identify how the number of available multipath influenced detection performance for an SNR of 5 dB in Fig. 8(b). Here, the available multipath refers to the multipath interacting with the target. The multipath component of the environment is fixed. So, increasing the number of target multipath components can increase the channel impulse response at multiple taps, and the covariance matrix of the distribution of hypothesis H1, i.e., targeted MPCs appearing in the received signal, also increases. Therefore, according to (19) - (23) and (25) we can obtain that the detection probability also increases, which is also consistent with the intuition. The detector is highly accurate with 10 available multipath.

### B. Performance of VA-Assisted Detection

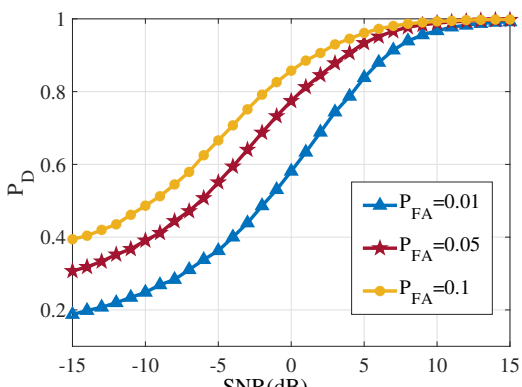
In this section, we illustrate the impacts of several errors as well as SNR on detection performance of two variant schemes. We consider the parameters in the real situation, which are listed in Table I.

We first explore the effect of the SNR on the detection performance of three schemes. Compared with the basic scheme, both VA-assisted schemes have better detection performance, especially when the demand for the false alarm is strict. In addition, the RIS-assisted scheme outperforms the multipath-assisted one.

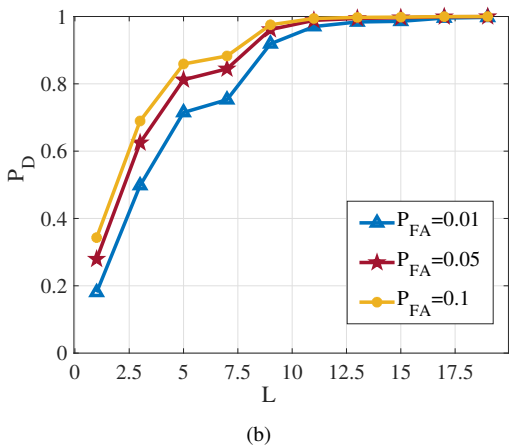
$$\max_{\psi_{p,n}} \left| \frac{\alpha_d \sqrt{K_r}}{\sqrt{K_r + 1}} \exp(-j\phi_d) + \sum_{p=1}^{P-1} \sum_{n=1}^{N_R} \frac{\alpha_{r,p}}{\sqrt{K_r + 1}} \exp(j\phi_{DA,p}(n) + j\psi_{p,n} - j\phi_{r,p}) \right|^2 = \max_{\psi_{p,n}} U \quad (80)$$

s.t.  $\omega_{p,n} = 1, \forall n = 1, \dots, N_R$

$$U \leq \left| \frac{\alpha_d \sqrt{K_r}}{\sqrt{K_r + 1}} \exp(-j\phi_d) \right| + \left| \sum_{p=1}^{P-1} \sum_{n=1}^{N_R} \frac{\alpha_{r,p}}{\sqrt{K_r + 1}} \exp(j\phi_{DA,p}(n) + j\psi_{p,n} - j\phi_{r,p}) \right| \quad (81)$$



(a)



(b)

Fig. 8. Detection probability versus (a) SNR and (b) the number of available multipath components. The detection probability increases with SNR and then converges to 1. Increasing the number of available multipath components can improve the detection probability.

TABLE I  
PARAMETERS FOR SIMULATION

Parameters	Value
False alarm rate $P_{FA}$	$10^{-2}$
Ephemeris error $\epsilon$	1.5m
VA position error $\sigma_{VA}$	0.5-1.5m
RIS error $\delta_{RIS}$	0.1-1.2m
Elevation angle $\theta$	5°, 30°, 80°
Atmospheric absorption $L_A(f, \theta)$	0-5dB
Excess path loss $\eta(\theta)$	5-10dB
PN code $N_{PN}$	1023
Bandwidth	20.45 MHz

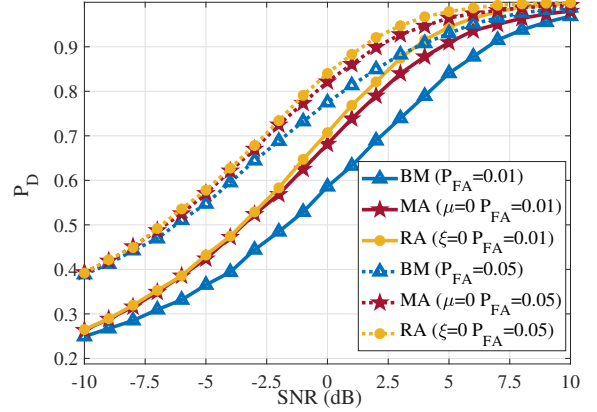


Fig. 9. Effect of SNR on detection probability of three schemes with different false alarm rates. Both VA-assisted schemes have better detection performance compared with the basic scheme. The RIS-assisted scheme outperforms the multipath-assisted one.

With the multipath-assisted scheme, we considered the effects of ephemeris error, VA position error, and path loss on detection accuracy. For the RIS-assisted scheme, we focused on ephemeris error, path loss, and RIS measurement error. The elevation angle affects atmospheric absorption loss as well as excess path loss. We thus regard the elevation angle's role in detection performance during our simulation. We specifically compare the two improved schemes' performance with that of the basic scheme. The basic scheme's performance is based on a false alarm rate of 0.01 and an SNR of 5 dB.

First, we analyze how VA position error influences detection performance in the multipath-assisted scheme. We use a special baseband structure that can simultaneously track multiple NLOS components along with the LOS component, such as MEDLL [43]. In such a structure, every multipath can be tracked independently. So the measurement error of the pseudo-range obtained from each multipath component is only decided by the bandwidth of the GNSS signal and the SNR of the corresponding multipath. Submeter-level accuracy can be obtained when the  $C/N_0$  exceeds 30 dB-Hz [44]. Fig. 10 shows that detection probability decreases as VA position error increases. The multipath-assisted scheme outperforms the basic scheme when the error is within about 1.2 m. In addition, the system also performs worse at small elevation angles.

In the RIS-assisted scheme, we evaluate the effect of RIS measurement errors on detection performance. According to [45], 90% positioning error is guaranteed to be less than 0.4 m,

even if the geometric dilution of precision at the RIS location is large. In Fig. 11, we compare this scheme's performance to that of the multipath-assisted and the basic schemes as measurement error increases. The multipath-assisted scheme is tested with an elevation angle of  $30^\circ$  and a VA position error of 0.5 m. The RIS-assisted scheme outperforms the basic and multipath-assisted schemes when the measurement error is within 1 m and 0.4 m, respectively. In addition, the 0.4 m RIS error is a prerequisite, which means that although RIS is not yet used widely in practice, the performance of the proposed RIS method will be better as long as the accuracy is achieved.

Then, we simulate the impacts of ephemeris errors on our two schemes' performance. The detection performance at different elevation angles versus ephemeris error appears in Fig. 12. The VA position error in the multipath-assisted scheme is set to 0.5 m, whereas the RIS measurement error is set to 0.1 m. The multipath-assisted scheme outperforms the basic one for an ephemeris error within 2.7 m; the RIS-assisted scheme outperforms the basic one for an ephemeris error within 3.6 m. Overall, the RIS-assisted scheme's detection accuracy exceeds that of the multipath-assisted scheme. In addition, the system demonstrates better detection performance for both variant schemes at high elevation angles.

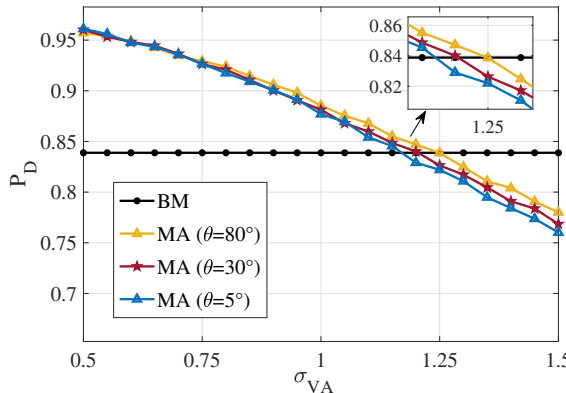


Fig. 10. Effect of RIS measurement error on detection probability of RIS-assisted scheme. The multipath-assisted scheme outperforms the basic scheme when the error is within about 1.2 m. The system performs worse at small elevation angles.

### C. Target Echo Optimization Simulation

In this section, the effect of the RIS-based target echo signal optimization on the detection performance will be verified by simulation. The SNR of the received signal without echo signal is set to 5 dB. The noise power is  $-109$  dBm. The RCS of the target is  $\sigma = 0.5$ . the wavelength is  $\lambda = 0.025$  m. The Rice factor is  $K_r = 5$  dB. The simulation scenario is shown in Fig. 13. The position of the receiver is set as the origin. Three RIS arrays are deployed, whose center coordinates are  $\mathbf{r}_{RIS,1} = [-155, -30, 30]^T$ ,  $\mathbf{r}_{RIS,2} = [150, 5, 30]^T$ ,  $\mathbf{r}_{RIS,3} = [10, 60, 25]^T$ , respectively. The coordinate of target position is  $\mathbf{r}_T = [50, 25, 200]^T$ .

Here, We add the consideration of echo signal SNR as part of the performance analysis. The echo signal SNR is different from the SNR mentioned above. Before RIS is introduced,

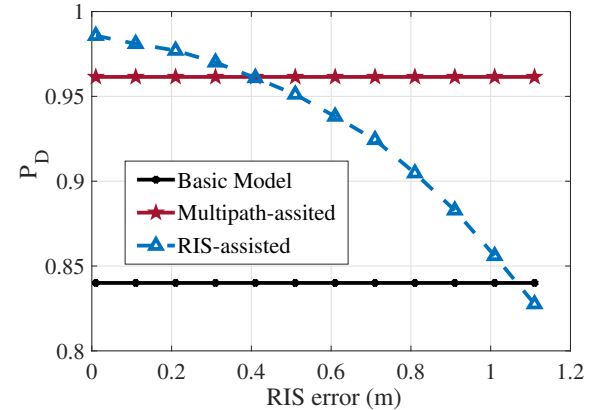


Fig. 11. Effect of RIS measurement error on detection probability of RIS-assisted scheme. The RIS-assisted scheme outperforms the basic and multipath-assisted schemes when the measurement error is within 1 m and 0.4 m, respectively.

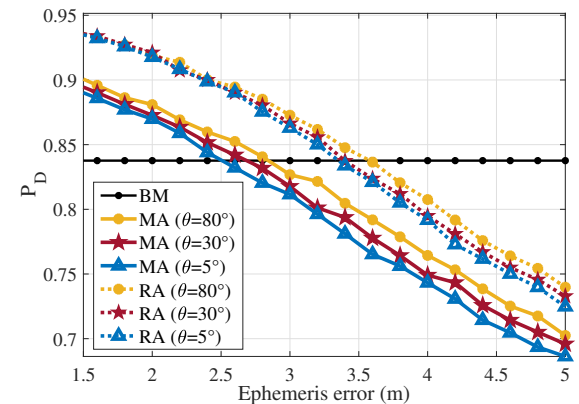


Fig. 12. Effect of ephemeris error on detection probability of three schemes. The multipath-assisted scheme outperforms the basic one for an ephemeris error within 2.7 m; the RIS-assisted scheme outperforms the basic one for an ephemeris error within 3.6 m. The RIS-assisted scheme's detection accuracy exceeds that of the multipath-assisted scheme. The system demonstrates better detection performance for both variant schemes at high elevation angles.

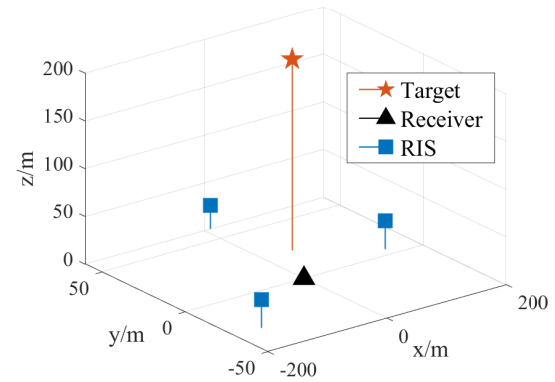


Fig. 13. Simulation scenario with 3 RIS and 1 target.

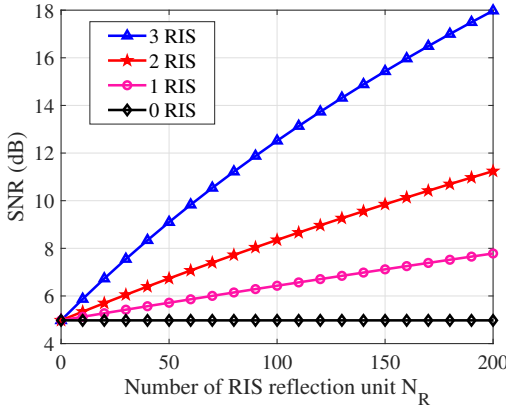


Fig. 14. Effect of the number of RIS array on SNR. Introducing RIS can improve the SNR, which increases further as the number of RIS.

the attenuation of the environmental MPC is relatively large, so the effect on the received signal SNR is small. The SNR approximates the LOS path SNR with a little loss. The LOS SNR can be set, so we treat the SNR as an adjustable parameter. However, the addition of RIS makes some changes. RIS can improve the reflection environment as well as the reflected MPC gain. Enhanced MPC improves the SNR at the receiver side, thus increasing the detection probability. Hence, the target echo SNR can be expressed as

$$SNR = \frac{\sum_{l=0}^{L-1} \sigma_{MPC}^2 |V[\tau_l - m\Delta T]|^2}{\sigma_w^2} + SNR_r. \quad (84)$$

where  $SNR_r$  is the SNR of the received signal without echo signal.

Fig. 14 shows the effect of the RIS array on the output SNR. As shown in the figure, the output SNR can be greatly improved by increasing the number of reflective elements in the RIS array. Moreover, the SNR also increases with the number of RIS array, especially when the number of RIS array is increased from 2 to 3. The reason is that the three RISs are evenly distributed around the receiver, and the range of RISs is wider. Although increasing the number of RIS and its reflection units can improve performance, the hardware implementation and deployment cost issues are necessary for practical use. We need to choose the number reasonably to achieve the best compromise in practice.

The effect of the RIS array on the detection probability is illustrated in Fig. 15. With no RIS array help, the detection probability only reaches 0.88 when the measurement error is 0.5 m and the ephemeris error is 3 m. It can be seen from the figure that designing the RIS profile can improve the detection probability. Furthermore, when three RIS arrays with 100 reflective elements are deployed, the detection probability can reach close to 1.

In addition, for targets in the regulatory area, the detection probability differs at different locations, and the RIS compensates the power differently. We take a plane with a 300 m vertical height as an example of the regulatory area. The detection probability distribution in the area is given in Fig.

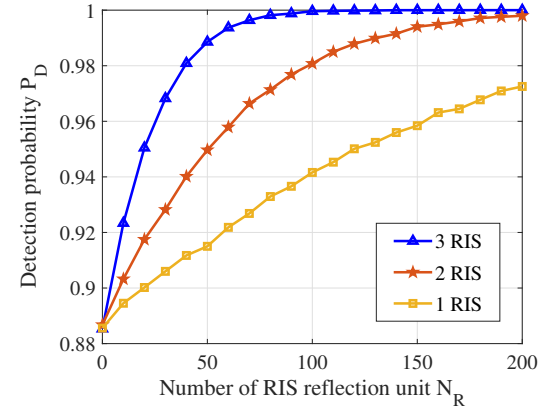


Fig. 15. Effect of the number of RIS array on detection probability. The detection performance is improved after designing the profile of RIS.

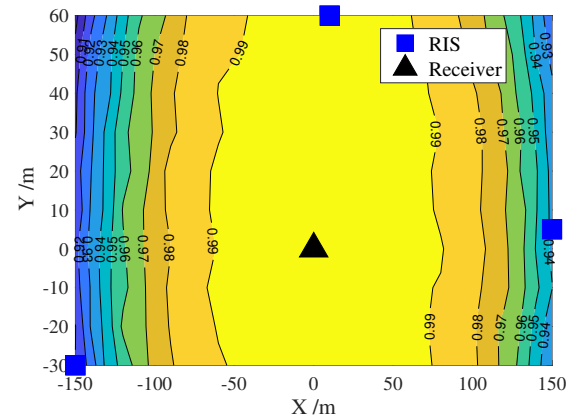


Fig. 16. Detection probability distribution of different locations. The closer the target is to the receiver, the higher the probability of detection.

16. As shown in the figure, the detection probability of a target at 300 m in the air is up to 90%. The detection probability increases as the distance between the target and the receiver decreases.

#### D. STK Simulation

STK, a software that can provide many real parameters, including satellite constellations, orbit parameters, elevation angles, azimuth angles, etc., is widely used for simulation analysis in multiple fields, such as satellite communications, radar detection, and electronic countermeasures. In this section, we use STK to perform simulation experiments.

The receiver is placed at 118°0'6" E, 24°35'15" N (Xiamen, China). GPS PRN1, PRN2, PRN3, and PRN5 are selected to validate the RIS-assisted scheme performance. The parameters are listed in Table. II.

We first use PRN1 to verify the detection performance of the RIS-assisted detection. The visible period of PRN1 is 04:16:34 - 10:58:38. We divide this period into ten moments equally. According to the recorded parameters, we can calculate the detection probability, which is shown in Fig. 17. The detection probability varies severely with the satellite moving. The

TABLE II  
PARAMETERS FOR STK SIMULATION

Parameters	Value
Transmitting power	25 W
Carrier frequency	1545.42 MHz
False alarm rate $P_{FA}$	$10^{-3}$
Ephemeris error $\epsilon$	3 m
RIS error $\delta_{RIS}$	0.2 m
PN code $N_{PN}$	1023
Reflection cross section	$0.5 \text{ m}^2$
Receiving antenna gain	25 dB
Coherence time	10 ms

maximum value is reached at moment 5 when the probability of detection is about 98.5%.

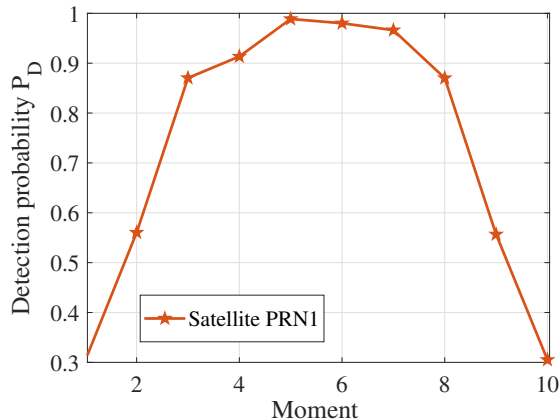


Fig. 17. Two-dimensional diagram of the multiple satellites orbits.

TABLE III  
SATELLITE VISIBILITY

No.	Start time (UTC)	End time (UTC)	Duration (sec)
PRN1	1 Jun 04:16:34.538	1 Jun 10:58:38.287	24123.750
PRN2	1 Jun 13:53:47.859	1 Jun 20:59:08.178	25520.318
PRN3	1 Jun 06:13:46.726	1 Jun 12:05:25.067	21098.341
	1 Jun 23:28:24.771	2 Jun 03:53:14.435	15889.664
PRN5	1 Jun 11:36:00.661	1 Jun 20:21:08.634	31507.973

We record the visible time of the selected satellite, as shown in Table III. We also evaluate the performance by using multiple satellites for comparison. The results are presented in Fig. 18. The figure shows that the cumulative proportion of detection probability by a single satellite is 7.2%, which increases to 41% by fusion detection with four satellites. Hence, as the number of satellites used for detection increases, the detection performance improves due to increased coverage area, which is also an advantage of GNSS signals compared to other illuminators.

## VII. CONCLUSION

In this paper, we describe LSS target detection as a binary hypothesis test based on variation in the received signal

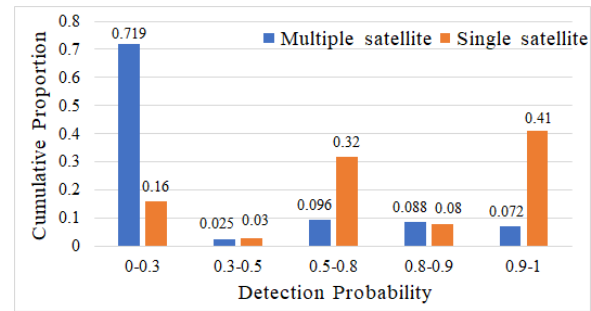


Fig. 18. Cumulative proportion of detection probabilities of single satellite scheme and multi-satellite fusion one. Increasing the number of satellites can improve the detection performance.

with the presence or absence of targets. An information-level target detection scheme is proposed as a foundation, and two performance indicators (i.e., false alarm rate and detection probability) are calculated theoretically. To use the multipath effect in complex urban environments, we introduce VA to convey reflected MPCs. The VAs' positions are estimated in the offline training phase, and then the environmental MPCs are predicted at the detection moment based on the estimated VAs. To artificially rebuild the reflective environment, we introduce RIS into our multipath-assisted scheme. Apart from simplifying VA estimation via geometric calculation, adding a RIS makes the received signal controllable in both signal processing and geometric propagation. We analyze test statistics and corresponding detection performance indicators under both schemes. Simulation results show that the detection probability of the multipath-assisted and RIS-assisted schemes could reach 90% and 94%, respectively, when the SNR is 5 dB. The performance gain brought by RIS is well-marked when the displacement error of RIS is less than 0.41 m. In addition, the output SNR can be greatly improved by increasing the number of RIS and reflective elements in the RIS array. To increase the realism of the simulation scenario, we use satellite tool kits (STK), a software that can provide realistic satellite parameters, to validate our methods.

The scenario experiments in this paper are relatively simple. More details need to be considered for application in the actual scenario. Therefore, future work will include a real experimental environment to further verify the application capability of the scheme in the actual environment. In addition, the RIS profile can be combined with the target detection accuracy for joint optimization design to enhance the system's sensing capability further. Target localization and tracking algorithm based on detection results is also a research direction.

## APPENDIX A DERIVATION OF THE DISTRIBUTION OF TEST STATISTIC

### A. Basic Scheme

The observation vector  $y$  follows a zero-mean complex Gaussian distribution under both hypotheses. According to Equation (20),  $x$  is a linear transformation of  $y$ ; therefore,  $x$  is also a zero-mean Gaussian random variable, such that

$E(\mathbf{x}) = 0$ . By substituting (20) into (11), the vector  $\mathbf{x}$  under  $\mathcal{H}_0$  obeys the following distribution:

$$\begin{aligned} \mathbf{x} | \mathcal{H}_0 &= \mathbf{D}_B^H \sqrt{\Lambda_w}^{-1} \mathbf{D}_w^H \mathbf{y} \\ &\sim \mathcal{CN}\left(0, \mathbf{D}_B^H \sqrt{\Lambda_w}^{-1} \mathbf{D}_w^H \mathbf{C}_w \mathbf{D}_w \sqrt{\Lambda_w}^{-1} \mathbf{D}_B\right) \\ &\sim \mathcal{CN}\left(0, \mathbf{D}_B^H \sqrt{\Lambda_w}^{-1} \Lambda_w \sqrt{\Lambda_w}^{-1} \mathbf{D}_B\right) \\ &\sim \mathcal{CN}(0, \mathbf{I}_M) \end{aligned} \quad (85)$$

Similarly, the distribution of  $\mathbf{x}$  under  $\mathcal{H}_1$  is given by

$$\begin{aligned} \mathbf{x} | \mathcal{H}_1 &\sim \mathcal{CN}\left[0, \mathbf{D}_B^H \Lambda_w^{-\frac{1}{2}} \mathbf{D}_w^H (\mathbf{C}_w + \mathbf{C}_v) \mathbf{D}_w \Lambda_w^{-\frac{1}{2}} \mathbf{D}_B\right] \\ &\sim \mathcal{CN}\left[0, \mathbf{I}_M + \mathbf{D}_B^H \left(\mathbf{D}_w \Lambda_w^{-\frac{1}{2}}\right)^H \mathbf{C}_v \mathbf{D}_w \Lambda_w^{-\frac{1}{2}} \mathbf{D}_B\right] \\ &\sim \mathcal{CN}(0, \mathbf{I}_M + \mathbf{D}_B^H \mathbf{B} \mathbf{D}_B) \\ &\sim \mathcal{CN}(0, \mathbf{I}_M + \boldsymbol{\Lambda}_B) \end{aligned} \quad (86)$$

Both the real part  $\text{Re}(x[m])$  and the imaginary part  $\text{Im}(x[m])$  are real Gaussian random variables and are independent of each other with the same variance (i.e., half of the variance of  $x[m]$ ). Consequently,  $|x[m]|^2 = \text{Re}^2(x[m]) + \text{Im}^2(x[m])$  follows a proportional chi-square distribution. (21) can then be rewritten as

$$T_{Basic}(\mathbf{x}) = \begin{cases} \sum_{m=0}^{M-1} \frac{\lambda_{B_m}}{2(\lambda_{B_m} + 1)} \left| \frac{x[m]}{1/\sqrt{2}} \right|^2, & \mathcal{H}_0 \\ \sum_{m=0}^{M-1} \frac{\lambda_{B_m}}{2} \left| \frac{x[m]}{\sqrt{(\lambda_{B_m} + 1)/2}} \right|^2, & \mathcal{H}_1 \end{cases} \quad (87)$$

where,

$$\begin{aligned} \frac{|x[m]|^2}{1/2} &\sim \chi_2^2, & \mathcal{H}_0 \\ \frac{|x[m]|^2}{(\lambda_{B_m} + 1)/2} &\sim \chi_2^2, & \mathcal{H}_1 \end{aligned} \quad (88)$$

The test statistic's distribution is

$$T_{Basic}(\mathbf{x}) \sim \sum_{m=0}^{M-1} \alpha_m \chi_2^2, \quad (89)$$

where

$$\alpha_m = \begin{cases} \frac{\lambda_{B_m}}{2(\lambda_{B_m} + 1)}, & \mathcal{H}_0 \\ \frac{\lambda_{B_m}}{2}, & \mathcal{H}_1 \end{cases}$$

### B. Multipath-assisted Scheme

To start, the mean of the observation vector  $\mathbf{x} = \mathbf{D}_v^H (\mathbf{y} - \mathbf{u}_\delta)$  is zero, wherein  $E(\mathbf{x}) = 0$ . The vector  $\mathbf{x}$  under  $\mathcal{H}_0$  then obeys the following distribution:

$$\begin{aligned} \mathbf{x} | \mathcal{H}_0 &= \mathbf{D}_v^H (\mathbf{y} - \mathbf{u}_\delta) \\ &\sim \mathcal{CN}\left(0, \mathbf{D}_v^H (\sigma_w^2 + \sigma_\delta^2) \mathbf{I}_M \mathbf{D}_v\right) \\ &\sim \mathcal{CN}(0, (\sigma_w^2 + \sigma_\delta^2) \mathbf{I}_M). \end{aligned} \quad (90)$$

Similarly, the distribution of  $\mathbf{x}$  under  $\mathcal{H}_1$  is given by

$$\begin{aligned} \mathbf{x} | \mathcal{H}_1 &\sim \mathcal{CN}(0, \mathbf{D}_v^H \mathbf{C}_{VA} \mathbf{D}_v) \\ &\sim \mathcal{CN}(0, \mathbf{D}_v^H (\mathbf{C}_v + (\sigma_w^2 + \sigma_\delta^2) \mathbf{I}_M) \mathbf{D}_v) \\ &\sim \mathcal{CN}(0, \boldsymbol{\Lambda}_v + (\sigma_w^2 + \sigma_\delta^2) \mathbf{I}_M). \end{aligned} \quad (91)$$

Based on (56), the test statistic can be rewritten as

$$T_{VA}(\mathbf{x}) = \begin{cases} \sum_{m=0}^{M-1} \frac{\lambda_{v_m} (\sigma_w^2 + \sigma_\delta^2)}{2(\lambda_{v_m} + \sigma_w^2 + \sigma_\delta^2)} \left| \frac{x[m]}{\sqrt{(\sigma_w^2 + \sigma_\delta^2)/2}} \right|^2, & \mathcal{H}_0 \\ \sum_{m=0}^{M-1} \frac{\lambda_{v_m}}{2} \left| \frac{x[m]}{\sqrt{(\lambda_{v_m} + (\sigma_w^2 + \sigma_\delta^2))/2}} \right|^2, & \mathcal{H}_1 \end{cases} \quad (92)$$

where,

$$\begin{aligned} \left| \frac{x[m]}{\sqrt{(\sigma_w^2 + \sigma_\delta^2)/2}} \right|^2 &\sim \chi_2^2, & \mathcal{H}_0 \\ \left| \frac{x[m]}{\sqrt{(\lambda_{v_m} + (\sigma_w^2 + \sigma_\delta^2))/2}} \right|^2 &\sim \chi_2^2, & \mathcal{H}_1 \end{aligned} \quad (93)$$

The test statistic's distribution is

$$T_{VA}(\mathbf{x}) \sim \sum_{m=0}^{M-1} \eta_m \chi_2^2, \quad (94)$$

where

$$\beta_m = \begin{cases} \frac{\lambda_{v_m} (\sigma_w^2 + \sigma_\delta^2)}{2(\lambda_{v_m} + \sigma_w^2 + \sigma_\delta^2)}, & \mathcal{H}_0 \\ \frac{\lambda_{v_m}}{2}, & \mathcal{H}_1 \end{cases}$$

Indicators for the RIS-assisted scheme are derived in a similar way as above; the derivation is thus not repeated here. The distribution is as follows:

$$T_{RIS}(\mathbf{x}) \sim \sum_{m=0}^{M-1} \eta_m \chi_2^2, \quad (95)$$

where

$$\eta_m = \begin{cases} \frac{\lambda_{v_m} \sigma_w^2}{2(\lambda_{v_m} + \sigma_w^2)}, & \mathcal{H}_0 \\ \frac{\lambda_{v_m}}{2}, & \mathcal{H}_1 \end{cases}$$

### REFERENCES

- [1] M. Mozaffari, W. Saad, M. Bennis, Y.-H. Nam, and M. Debbah, "A tutorial on uavs for wireless networks: Applications, challenges, and open problems," *IEEE communications surveys & tutorials*, vol. 21, no. 3, pp. 2334–2360, 2019.
- [2] H. D. Griffiths and C. J. Baker, *An introduction to passive radar*. Artech House, 2022.
- [3] F. Colone, "Dvb-t-based passive forward scatter radar: Inherent limitations and enabling solutions," *IEEE Transactions on Aerospace and Electronic Systems*, vol. 57, no. 2, pp. 1084–1104, 2021.
- [4] W. Nie, Z.-C. Han, M. Zhou, L.-B. Xie, and Q. Jiang, "Uav detection and identification based on wifi signal and rf fingerprint," *IEEE Sensors Journal*, vol. 21, no. 12, pp. 13 540–13 550, 2021.
- [5] Y. Li, X. Wang, and Z. Ding, "Multi-target position and velocity estimation using ofdm communication signals," *IEEE Transactions on Communications*, vol. 68, no. 2, pp. 1160–1174, 2019.
- [6] P. Samczyński, K. Abratkiewicz, M. Płotka, T. P. Zieliński, J. Wszolek, S. Hausman, P. Korbel, and A. Ksieżyk, "5g network-based passive radar," *IEEE Transactions on Geoscience and Remote Sensing*, vol. 60, pp. 1–9, 2021.
- [7] C. Huang, Z. Li, H. An, Z. Sun, J. Wu, and J. Yang, "Passive multistatic radar imaging of vessel target using gnss satellites of opportunity," *IEEE Transactions on Geoscience and Remote Sensing*, vol. 60, pp. 1–16, 2022.
- [8] X. Zhou, P. Wang, H. Zeng, and J. Chen, "Moving target detection using gnss-based passive bistatic radar," *IEEE Transactions on Geoscience and Remote Sensing*, vol. 60, pp. 1–15, 2022.

- [9] F. Santi, F. Pieralice, and D. Pastina, "Joint detection and localization of vessels at sea with a gnss-based multistatic radar," *IEEE Transactions on Geoscience and Remote Sensing*, vol. 57, no. 8, pp. 5894–5913, 2019.
- [10] B. J. Southwell, J. W. Cheong, and A. G. Dempster, "A matched filter for spaceborne gnss-r based sea-target detection," *IEEE Transactions on Geoscience and Remote Sensing*, vol. 58, no. 8, pp. 5922–5931, 2020.
- [11] J. W. Cheong, B. J. Southwell, and A. G. Dempster, "Blind sea clutter suppression for spaceborne gnss-r target detection," *IEEE Journal of Selected Topics in Applied Earth Observations and Remote Sensing*, vol. 12, no. 12, pp. 5373–5378, 2019.
- [12] H. Bolvardi, M. Derakhtian, and A. Sheikhi, "Dynamic clutter suppression and multitarget detection in a dvb-t-based passive radar," *IEEE Transactions on Aerospace and Electronic Systems*, vol. 53, no. 4, pp. 1812–1825, 2017.
- [13] Y. Li, S. Yan, and J. Gong, "Target detection and location by fusing delay-doppler maps," *IEEE Transactions on Geoscience and Remote Sensing*, 2022.
- [14] H. Chen, H. Sarieddeen, T. Ballal, H. Wymeersch, M.-S. Alouini, and T. Y. Al-Naffouri, "A tutorial on terahertz-band localization for 6g communication systems," *IEEE Communications Surveys & Tutorials*, vol. 24, no. 3, pp. 1780–1815, 2022.
- [15] E. M. Vitucci, J. Chen, V. Degli-Esposti, J. S. Lu, H. L. Bertoni, and X. Yin, "Analyzing radio scattering caused by various building elements using millimeter-wave scale model measurements and ray tracing," *IEEE Transactions on Antennas and Propagation*, vol. 67, no. 1, pp. 665–669, 2019.
- [16] R. Mendrzik, H. Wymeersch, G. Bauch, and Z. Abu-Shaban, "Harnessing nlos components for position and orientation estimation in 5g millimeter wave mimo," *IEEE Transactions on Wireless Communications*, vol. 18, no. 1, pp. 93–107, 2019.
- [17] E. Leitinger, F. Meyer, F. Hlawatsch, K. Witrisal, F. Tufvesson, and M. Z. Win, "A belief propagation algorithm for multipath-based slam," *IEEE Transactions on Wireless Communications*, vol. 18, no. 12, pp. 5613–5629, 2019.
- [18] J. Yang, C.-K. Wen, and S. Jin, "Hybrid active and passive sensing for slam in wireless communication systems," *IEEE Journal on Selected Areas in Communications*, vol. 40, no. 7, pp. 2146–2163, 2022.
- [19] L.-T. Hsu, "Analysis and modeling gps nlos effect in highly urbanized area," *GPS solutions*, vol. 22, no. 1, pp. 1–12, 2018.
- [20] X. Chen, Y. J. Morton, W. Yu, and T.-K. Truong, "Gps 11ca/bds b1i multipath channel measurements and modeling for dynamic land vehicle in shanghai dense urban area," *IEEE Transactions on Vehicular Technology*, vol. 69, no. 12, pp. 14 247–14 263, 2020.
- [21] W. Wen and L.-T. Hsu, "3d lidar aided gnss nlos mitigation in urban canyons," *IEEE Transactions on Intelligent Transportation Systems*, 2022.
- [22] A. Al-Hourani and I. Guvenc, "On modeling satellite-to-ground path-loss in urban environments," *IEEE Communications Letters*, vol. 25, pp. 696–700, 2021.
- [23] H. Dong, C. Hua, L. Liu, and W. Xu, "Towards integrated terrestrial-satellite network via intelligent reflecting surface," *ICC 2021 - IEEE International Conference on Communications*, pp. 1–6, 2021.
- [24] M. di Renzo, A. Zappone, M. Debbah, M.-S. Alouini, C. Yuen, J. de Rosny, and S. A. Tretyakov, "Smart radio environments empowered by reconfigurable intelligent surfaces: How it works, state of research, and the road ahead," *IEEE Journal on Selected Areas in Communications*, vol. 38, pp. 2450–2525, 2020.
- [25] H. Wymeersch, J. He, B. Denis, A. Clemente, and M. J. Juntti, "Radio localization and mapping with reconfigurable intelligent surfaces: Challenges, opportunities, and research directions," *IEEE Vehicular Technology Magazine*, vol. 15, pp. 52–61, 2019.
- [26] E. Björnson, Ö. Özdogan, and E. G. Larsson, "Reconfigurable intelligent surfaces: Three myths and two critical questions," *IEEE Communications Magazine*, vol. 58, pp. 90–96, 2020.
- [27] Q. Wu, S. Zhang, B. Zheng, C. You, and R. Zhang, "Intelligent reflecting surface-aided wireless communications: A tutorial," *IEEE Transactions on Communications*, vol. 69, pp. 3313–3351, 2020.
- [28] Q. Wu and R. Zhang, "Towards smart and reconfigurable environment: Intelligent reflecting surface aided wireless network," *IEEE Communications Magazine*, vol. 58, pp. 106–112, 2019.
- [29] M. D. Renzo, M. Debbah, D.-T. Phan-Huy, A. Zappone, M.-S. Alouini, C. Yuen, V. Sciancalepore, G. C. Alexandropoulos, J. Hoydis, H. Gacanin *et al.*, "Smart radio environments empowered by reconfigurable ai meta-surfaces: an idea whose time has come," *EURASIP Journal on Wireless Communications and Networking*, vol. 2019, pp. 1–20, 2019.
- [30] E. Björnson, H. Wymeersch, B. Matthiesen, P. Popovski, L. Sanguinetti, and E. de Carvalho, "Reconfigurable intelligent surfaces: A signal processing perspective with wireless applications," *IEEE Signal Processing Magazine*, vol. 39, pp. 135–158, 2021.
- [31] K. Tekbiyik, G. K. Kurt, A. R. Ekti, and H. Yanikomeroglu, "Reconfigurable intelligent surfaces in action for nonterrestrial networks," *IEEE Vehicular Technology Magazine*, vol. 17, no. 3, pp. 45–53, 2022.
- [32] S. Xu, J. Liu, Y. Cao, J. Li, and Y. Zhang, "Intelligent reflecting surface enabled secure cooperative transmission for satellite-terrestrial integrated networks," *IEEE Transactions on Vehicular Technology*, vol. 70, pp. 2007–2011, 2021.
- [33] B. Zheng, S. Lin, and R. Zhang, "Intelligent reflecting surface-aided leo satellite communication: Cooperative passive beamforming and distributed channel estimation," *IEEE Journal on Selected Areas in Communications*, vol. 40, pp. 3057–3070, 2022.
- [34] Y. J. Morton, F. van Diggelen, J. J. Spilker Jr, B. W. Parkinson, S. Lo, and G. Gao, *Position, navigation, and timing technologies in the 21st century: Integrated satellite navigation, sensor systems, and civil applications, volume 1*. John Wiley & Sons, 2021.
- [35] X. Xu, A. Peng, and X. Hong, "Unscented kalman filtering based multipath-assisted positioning with peak flow tracking," in *2022 IEEE 12th International Conference on Indoor Positioning and Indoor Navigation (IPIN)*. IEEE, 2022, pp. 1–8.
- [36] X. Li, E. Leitinger, M. Oskarsson, K. Åström, and F. Tufvesson, "Massive mimo-based localization and mapping exploiting phase information of multipath components," *IEEE transactions on wireless communications*, vol. 18, no. 9, pp. 4254–4267, 2019.
- [37] P. Billingsley, *Convergence of probability measures*. John Wiley & Sons, 2013.
- [38] A. Franklin, *Introduction to the Theory of Statistics*, 1974.
- [39] Y. Chen, S. Yan, and J. Gong, "Phase error analysis and compensation of geo-satellite-based gnss-r deformation retrieval," *IEEE Geoscience and Remote Sensing Letters*, vol. 19, pp. 1–5, 2022.
- [40] A. Al-Hourani and I. Guvenc, "On modeling satellite-to-ground path-loss in urban environments," *IEEE Communications Letters*, vol. 25, no. 3, pp. 696–700, 2021.
- [41] X. D. Zhang, "Matrix analysis and applications," 2017.
- [42] Ö. Özdogan, E. Björnson, and E. G. Larsson, "Intelligent reflecting surfaces: Physics, propagation, and pathloss modeling," *IEEE Wireless Communications Letters*, vol. 9, no. 5, pp. 581–585, 2020.
- [43] M. Sánchez-Fernández, M. Aguilera-Forero, and A. García-Armada, "Performance analysis and parameter optimization of dll and medll in fading multipath environments for next generation navigation receivers," *IEEE Transactions on Consumer Electronics*, vol. 53, no. 4, pp. 1302–1308, 2007.
- [44] N. Blanco-Delgado and F. D. Nunes, "Multipath estimation in multicorrelator gnss receivers using the maximum likelihood principle," *IEEE Transactions on Aerospace and Electronic Systems*, vol. 48, no. 4, pp. 3222–3233, 2012.
- [45] K. Keykhsravi, M. F. Keskin, S. Dwivedi, G. Seco-Granados, and H. Wymeersch, "Semi-passive 3d positioning of multiple ris-enabled users," *IEEE Transactions on Vehicular Technology*, vol. 70, no. 10, pp. 11 073–11 077, 2021.



**Xueling Xu** received the B.S. degree from Nanjing University of Science and Technology, Nanjing, China. She is currently pursuing the Ph.D. degree in communication and information system at Xiamen University, China. Her research interests include wireless communications, multipath-assisted positioning, optimal state estimation.



**Yang Zhou** received the B.S. degree from Fuzhou University. He received the M.S. degree from the School of Informatics, Xiamen University, Xiamen, China. His research interests include target detection, integrated sensing and communication.



**Qi Yang** received the B.E. and M.S. degrees from the Department of Communication Engineering, Fuzhou University, Fuzhou, China, in 2000 and 2003, respectively, and the Ph.D. degree from the Department of Communication Engineering, Xiamen University, Xiamen, China, in 2008. From 2003 to 2005, he was a Teaching Assistant with the School of Information Science and Technology, Fuzhou University. From 2008 to 2015, he was an Assistant Professor with the School of Information Science and Technology, Xiamen University. From 2016 to 2019, he visited the Department of Electrical and Computer Engineering, University of Waterloo, Canada, and the Department of Engineering Science, National Cheng Kung University, Taiwan. He is currently an Associate Professor with the School of Informatics, Xiamen University. His research interest includes wideband wireless communication and networks.



**Huiying Li** received the B.E. degree from Nanjing University of Posts and Telecommunications, Nanjing, China. She is currently pursuing the M.Sc degree in communication engineering at Xiamen University, China. Her research interests include wireless communications, indoor positioning.



**Ao Peng** received the M.Sc degree and the Ph.D in Communication and Information System from Xiamen University, Fujian, China, in 2011 and 2014, respectively. In 2015, he joined the School of Informatics, Xiamen University, where he is currently an Assistant Professor. His research interests including satellite navigation, indoor navigation and multi-source positioning and navigation.



**Qiang (John) Ye** received the PhD degree in Electrical and Computer Engineering from the University of Waterloo, ON, Canada, in 2016. Since Sept. 2023, he has been an Assistant Professor with the Department of Electrical and Software Engineering, University of Calgary, AB, Canada. Before joining UCalgary, he worked as an Assistant Professor with the Department of Computer Science, Memorial University of Newfoundland, NL, Canada from Sept. 2021 to Aug. 2023 and with the Department of Electrical and Computer Engineering and Technology,

Minnesota State University, USA, from Sept. 2019 to Aug. 2021, respectively. He was with the Department of Electrical and Computer Engineering, University of Waterloo as a Postdoctoral Fellow and then a Research Associate from Dec. 2016 to Sept. 2019. He has published over 60 research articles on top-ranked IEEE Journals and Conference Proceedings. He is/was General and TPC co-chairs for different international conferences and workshops, e.g., IEEE VTC'22, IEEE INFOCOM'22, and IEEE IPCCC'21. He serves/served as Associate Editors of IEEE Transactions on Cognitive Communications and Networking, IEEE Open Journal of the Communications Society, Peer-to-Peer Networking and Applications, ACM/Wireless Networks, and International Journal of Distributed Sensor Networks. He also serves as the IEEE Vehicular Technology Society (VTS) Regions 1-7 Chapters Coordinator (2022-2023). He is a Senior Member of IEEE.